PHYSICAL REVIEW C **83**, 045810 (2011)

Core-crust transition in neutron stars: Predictivity of density developments

Camille Ducoin,[1] Jérôme Margueron,[2] Constança Providência,[1] and Isaac Vidaña[1]
[1]*CFC, Department of Physics, University of Coimbra, PT-3004-516, Coimbra, Portugal*
[2]*Institut de Physique Nucléaire, Université Paris-Sud, IN2P3-CNRS, FR-91406 Orsay Cedex, France*

(Received 2 February 2011; published 28 April 2011)

The possibility to draw links between the isospin properties of nuclei and the structure of compact stars is a stimulating perspective. In order to pursue this objective on a sound basis, the correlations from which such links can be deduced have to be carefully checked against model dependence. Using a variety of nuclear effective models and a microscopic approach, we study the relation between the predictions of a given model and those of a Taylor density development of the corresponding equation of state: this establishes to what extent a limited set of phenomenological constraints can determine the core-crust transition properties. From a correlation analysis, we show that (a) the transition density ρ_t is mainly correlated with the symmetry energy slope L, (b) the proton fraction $Y_{p,t}$ with the symmetry energy and symmetry energy slope (J, L) defined at saturation density, or, even better, with the same quantities defined at $\rho = 0.1$ fm^{-3}, and (c) the transition pressure P_t with the symmetry energy slope and curvature (L, K_{sym}) defined at $\rho = 0.1$ fm^{-3}.

DOI: 10.1103/PhysRevC.83.045810 PACS number(s): 26.60.Gj, 21.65.Ef, 21.30.Fe

I. INTRODUCTION

The study of nuclear systems under extreme conditions is an expanding field of research involving astrophysical processes, laboratory experiments with rare-isotope beams, and the development of more realistic nuclear models. The density dependence of the symmetry energy $S(\rho)$ is one of the central issues in this field [1–3]. Although the symmetry energy at saturation density ρ_0 is considered to be well known [$J = S(\rho_0) = 33 \pm 3$ MeV], the different nuclear models present a wide range of predictions for the symmetry energy slope $L = 3\rho_0[\partial S/\partial\rho](\rho_0)$. Several experimental observables have been proposed to obtain a measure of L, for instance, neutron-skin thickness [4], isovector dipolar resonances [5,6], isoscaling in multifragmentation [7], and isospin diffusion [8]. The perspective to obtain more stringent constraints on the value of L has motivated several studies concerning the impact of this quantity on compact star structure, especially on the characterization of the core-crust transition in neutron stars [9–11]. In a previous work [12], we have addressed the model dependence of the link between L and the core-crust transition properties: density ρ_t, proton fraction $Y_{p,t}$, and pressure P_t. It appeared that ρ_t and $Y_{p,t}$ are unambiguously correlated with L, while the link between L and P_t is very sensitive to the model. The transition pressure is the dominant input for the prediction of one of the most important crust properties, namely, the moment of inertia of the crust that may affect pulsar glitches [13,14]. It is then an important challenge to find a better relation between P_t and laboratory data.

In this paper, we investigate the role of symmetry-energy properties other than L that could also, hopefully, be related to laboratory data. To perform this study, we use (as previously) several Skyrme and relativistic effective models and a microscopic Brueckner-Hartree-Fock (BHF) approach. We also employ a schematic nuclear equation of state (EOS), based on a density development around a reference density, that we call the generalized liquid-drop model (GLDM): our objective is to establish to what extent the core-crust transition obtained with a given nuclear model can be reproduced with a limited set of GLDM coefficients. In other words, we investigate how the specificities of each model can affect the link between phenomenological constraints (i.e., the set of GLDM coefficients, which could be determined from laboratory data) and the core-crust transition.

In this paper, the core-crust transition properties are first calculated in the thermodynamic framework, with the transition defined as the crossing between the β-equilibrium line and the thermodynamic spinodal border. The thermodynamic spinodal corresponds to the bulk instability of homogeneous nuclear matter. In fact, in a compact star at the core-crust transition, the ground state of stellar matter changes from a clusterized configuration (lattice of nuclei, or more exotic structures named pasta phases [2,15,16]) to homogeneous matter. It has been shown that this transition can be very well approximated by the crossing between β equilibrium and the dynamic spinodal border [17], which corresponds to the finite-size instability region of homogeneous matter: Coulomb and surface contributions make the dynamic spinodal smaller than the thermodynamic one [18–20]. Therefore, we also address the dynamic core-crust transition properties, which are strongly correlated with the thermodynamic ones.

This paper is organized as follows. The generalized liquid-drop model is presented in Sec. II. We discuss the correlations existing between various GLDM coefficients and evaluate the accuracy of the core-crust transition predictions obtained with different GLDM expansions. In Sec. III, we present in more details the analysis of the link between the symmetry-energy slope at saturation L and the core-crust transition, which was first presented in Ref. [12]. In Sec. IV, we perform a correlation analysis involving coefficients other than L. This allows us to establish relations between selected GLDM coefficients and realistic transition properties, within a reduced range of model dispersion. Conclusions are presented in Sec. V.

II. GENERALIZED LIQUID-DROP MODEL

Nuclear density functionals allow us to calculate the nuclear matter equation of state for any total density $\rho = \rho_n + \rho_p$ and asymmetry $y = (\rho_n - \rho_p)/(\rho_n + \rho_p)$. They may also present a complex dependence on the density, including, for instance, kinetic densities, spin densities, and density gradients. Such functionals can be derived from different nuclear models. In this paper, we consider Skyrme and relativistic effective models as well as an equation of state based on BHF calculations. These models, presented in the Appendix, are referred to as complete functionals, in contrast with the GLDM that is presented in this section.

The GLDM corresponds to a series expansion of the EOS around a given reference density. It is determined by three choices : (i) the nuclear model giving the full equation of state $E(\rho, y)$, (ii) the reference density $\rho_{\rm ref}$, and (iii) the order $\mathcal{N}$ of the development. The order $\mathcal{N}$ and the reference density ($\rho_{\rm ref}$) can be chosen at will. In this paper, the GLDM coefficients are derived from the complete EOS $E(\rho, y)$ given by various nuclear models. In a different context, the GLDM coefficients could be nuclear properties determined experimentally at $\rho_{\rm ref}$, from which we would extrapolate the nuclear EOS at lower or higher densities. We introduce the GLDM in order to investigate how well such an extrapolation allows us to reproduce the core-crust transition predicted by the complete functional, in other words, to what extent the role of higher-order terms can be neglected. Comparing the GLDM predictions with the results from the corresponding complete functional shows how much a more detailed density dependence of the EOS may affect these predictions.

A. GLDM equation of state

For a given reference density $\rho_{\rm ref}$ and order of development $\mathcal{N}$, the GLDM energy per particle reads as

$$E_{\rm GLDM}(\rho, y) = \sum_{n=0}^{\mathcal{N}} (c_{{\rm IS},n} + c_{{\rm IV},n}\, y^2)\frac{x^n}{n!} + \left(E_{\rm kin} - E_{\rm kin}^{\rm para}\right)$$
$$\text{with} \quad x = \frac{\rho - \rho_{\rm ref}}{3\rho_{\rm ref}}. \qquad (1)$$

The first term on the right-hand side of Eq. (1) contains both the kinetic and the potential contributions to the energy in the parabolic approximation with respect to the asymmetry y. The second term gives the contribution of the kinetic term beyond the parabolic approximation, as it will be explained below. We have introduced in this expression the GLDM coefficients $c_{{\rm IS},n}$ and $c_{{\rm IV},n}$, associated respectively with the derivatives of the energy $E(\rho, y = 0)$ and of the symmetry energy $S(\rho)$: the index IS (IV) stands for isoscalar (isovector). They are expressed as

$$c_{{\rm IS},n}(\rho_{\rm ref}) = (3\rho_{\rm ref})^n \frac{\partial^n E}{\partial \rho^n}(\rho_{\rm ref}, 0), \qquad (2)$$

$$c_{{\rm IV},n}(\rho_{\rm ref}) = (3\rho_{\rm ref})^n \frac{\partial^n S}{\partial \rho^n}(\rho_{\rm ref}) \quad \text{with} \quad S(\rho) = \frac{1}{2}\frac{\partial^2 E}{\partial y^2}(\rho, 0). \qquad (3)$$

In the case $\rho_{\rm ref} = \rho_0$, the lower-order coefficients are usual nuclear matter properties: $c_{{\rm IS},0} = E_0$ (saturation energy), $c_{{\rm IS},2} = K_0$ (incompressibility), $c_{{\rm IS},3} = Q_0$, $c_{{\rm IV},0} = J$ (symmetry energy), $c_{{\rm IV},1} = L$ (symmetry-energy slope), $c_{{\rm IV},2} = K_{\rm sym}$ (symmetry incompressibility), and $c_{{\rm IV},3} = Q_{\rm sym}$.

The parabolic approximation, which restricts Eq. (1) to the first term, is known to be quite accurate to describe the EOS even at high isospin asymmetry. However, it fails to reproduce the spinodal contour in the neutron-rich region. The reason is that the energy-density curvature in the proton-density direction must diverge at small proton density because of the kinetic term (see the appendix of Ref. [21]); as a result, the spinodal contour can not reach pure neutron matter. Instead, in the parabolic approximation, the curvature in the proton-density direction is constant and leads to the unphysical prediction of unstable neutron matter. To avoid this discrepancy, we have introduced in Eq. (1) a model-independent correction based on the nonrelativistic, free Fermi gas kinetic term

$$E_{\rm kin} = \frac{1}{\rho}\left[\frac{\hbar^2}{2m}(\tau_n + \tau_p)\right], \qquad (4)$$

where $\tau_q = (3\pi^2\rho_q)^{5/3}/(5\pi^2)$ is the kinetic density of the nucleon species $q = n, p$ and m is the nucleon mass. As a function of density and asymmetry, we have

$$E_{\rm kin} = \frac{(3\pi^2/2)^{5/3}}{10m\pi^2}\rho^{2/3}[(1+y)^{5/3} + (1-y)^{5/3}], \qquad (5)$$

$$E_{\rm kin}^{\rm para} = \frac{(3\pi^2/2)^{5/3}}{10m\pi^2}\rho^{2/3}\left[2 + \frac{10}{9}y^2\right], \qquad (6)$$

where $E_{\rm kin}^{\rm para}$ is the parabolic part of $E_{\rm kin}$. In the GLDM defined by Eq. (1), the extra-parabolic behavior of the functional is sketched by the extra-parabolic behavior of $E_{\rm kin}$, which brings the model-independent correction $E_{\rm kin} - E_{\rm kin}^{\rm para}$ [second term on the right-hand side of Eq. (1)].

In the following, we will use the notation $D_{\mathcal{N}}(\rho_{\rm ref})$ to identify a development of order $\mathcal{N}$ around the density $\rho_{\rm ref}$. Developments of this kind are usually considered up to $\mathcal{N} = 3$, around the saturation density $\rho_0 \simeq 0.16$ fm^{-3} (see, e.g., Refs. [22,23]). In this paper, we will also consider an extreme situation labeled D_∞. Performing an infinite development gives the exact value of $E(\rho, 0)$ and $S(\rho)$ for any density ρ, whatever the choice of $\rho_{\rm ref}$. In practice, the D_∞ equation of state is simply built using the exact expressions of $E(\rho, 0)$ and $S(\rho)$ to obtain $E(\rho, y)$:

$$E_{D_\infty}(\rho, y) = E(\rho, 0) + S(\rho)y^2 + \left(E_{\rm kin} - E_{\rm kin}^{\rm para}\right). \qquad (7)$$

Thus, the difference between a complete functional and its associated D_∞ model is just the extra-parabolic content of the nuclear interaction, which has not been taken into account by the correction $E_{\rm kin} - E_{\rm kin}^{\rm para}$ defined above. Let us note that a parabolic approximation is often assumed in BHF calculations to interpolate between the symmetric-matter and neutron-matter EOS. We will call this approach BHF$_{\rm para}$. However, by default, our BHF results include the correction $E_{\rm kin} - E_{\rm kin}^{\rm para}$; in this case, the complete functional is exactly equivalent to the corresponding D_∞ model.

TABLE I. GLDM coefficients at saturation density ρ_0 and at $\rho_{\rm ref} = 0.1$ fm^{-3} for different nuclear models. Details and references concerning these models are given in the Appendix. BHF-1: Functional fit includes calculation points in the density range $\rho = [0.1; 0.35]$ fm^{-3}. BHF-2: functional fit includes calculation points in the density range $\rho = [0.05; 0.18]$ fm^{-3}. The coefficients are named following traditional notations. Isoscalar coefficients at saturation density: $E_0 = c_{\rm IS,0}$, $K_0 = c_{\rm IS,2}$, $Q_0 = c_{\rm IS,3}$. Isovector coefficients at saturation density: $J = c_{\rm IV,0}$, $L = c_{\rm IV,1}$, $K_{\rm sym} = c_{\rm IV,2}$, $Q_{\rm sym} = c_{\rm IV,3}$. Isoscalar coefficients at $\rho_{\rm ref} = 0.1$ fm^{-3}: $E_{01} = c_{\rm IS,0}$, $L_{\rm IS,01} = c_{\rm IS,1}$, $K_{01} = c_{\rm IS,2}$. Isovector coefficients at $\rho_{\rm ref} = 0.1$ fm^{-3}: $J_{01} = c_{\rm IV,0}$, $L_{01} = c_{\rm IV,1}$, $K_{\rm sym,01} = c_{\rm IV,2}$.

Model	ρ_0 (fm^{-3})	E_0 (MeV)	K_0 (MeV)	Q_0 (MeV)	J (MeV)	L (MeV)	$K_{\rm sym}$ (MeV)	$Q_{\rm sym}$ (MeV)	E_{01} (MeV)	$L_{\rm IS,01}$ (MeV)	K_{01} (MeV)	J_{01} (MeV)	L_{01} (MeV)	$K_{\rm sym,01}$ (MeV)
Microscopic														
BHF-1	0.187	−15.23	195.50	−280.90	34.30	66.55	−31.30	−112.80	−12.72	−17.58	62.62	22.77	40.14	−28.45
BHF-2									−12.74	−17.59	67.01	22.77	41.35	−44.30
Skyrme														
BSk14	0.159	−15.86	239.38	−358.78	30.00	43.91	−152.03	388.30	−13.92	−20.65	118.58	23.29	41.94	−89.79
BSk16	0.159	−16.06	241.73	−363.69	30.00	34.87	−187.39	461.93	−14.10	−20.87	119.86	24.11	39.44	−109.16
BSk17	0.159	−16.06	241.74	−363.73	30.00	36.28	−181.86	450.52	−14.10	−20.87	119.87	23.98	39.83	−106.13
G_σ	0.158	−15.59	237.29	−348.82	31.37	94.02	13.99	−26.77	−13.71	−20.31	118.13	20.03	58.46	6.62
R_σ	0.158	−15.59	237.41	−348.50	30.58	85.70	−9.13	22.23	−13.71	−20.34	117.99	20.05	55.22	−6.21
LNS	0.175	−15.32	210.83	−382.67	33.43	61.45	−127.37	302.48	−12.96	−20.07	95.92	23.20	48.07	−66.20
NRAPR	0.161	−15.86	225.70	−362.65	32.78	59.63	−123.33	311.63	−13.93	−19.89	112.26	24.18	48.86	−72.09
RATP	0.160	−16.05	239.58	−349.94	29.26	32.39	−191.25	440.74	−14.05	−20.78	116.94	23.55	38.04	−108.29
SV	0.155	−16.05	305.75	−175.86	32.82	96.10	24.19	47.97	−13.86	−24.15	135.63	21.60	60.45	5.26
SGII	0.158	−15.60	214.70	−381.02	26.83	37.62	−145.92	330.44	−13.84	−18.91	111.74	20.98	37.16	−83.35
SkI2	0.158	−15.78	240.99	−339.81	33.38	104.35	70.71	51.60	−13.88	−20.54	119.16	21.17	61.18	22.73
SkI3	0.158	−15.99	258.25	−303.96	34.83	100.53	73.07	211.53	−13.96	−21.66	122.84	23.03	59.52	11.04
SkI4	0.160	−15.95	247.98	−331.26	29.50	60.40	−40.52	351.09	−13.88	−21.33	118.11	21.48	43.25	−43.97
SkI5	0.156	−15.85	255.85	−302.05	36.64	129.34	159.60	11.71	−13.93	−21.22	124.33	22.33	71.01	62.14
SkI6	0.159	−15.92	248.65	−327.44	30.09	59.70	−47.27	378.96	−13.90	−21.23	119.31	22.19	43.70	−48.82
SkMP	0.157	−15.57	230.93	−338.15	29.89	70.31	−49.82	159.44	−13.76	−19.72	116.03	20.95	49.62	−32.93
SkO	0.160	−15.84	223.39	−392.98	31.97	79.14	−43.17	131.12	−13.93	−19.87	113.35	21.63	53.60	−27.51
Sly230a	0.160	−15.99	229.94	−364.29	31.98	44.31	−98.21	602.92	−14.06	−20.16	114.48	25.43	39.40	−86.38
Sly230b	0.160	−15.98	229.96	−363.21	32.01	45.96	−119.72	521.54	−14.06	−20.11	114.87	25.15	41.58	−88.09
SLy4	0.160	−15.98	229.97	−363.22	32.00	45.94	−119.74	521.58	−14.06	−20.11	114.87	25.15	41.56	−88.09
SLy10	0.156	−15.91	229.74	−358.43	31.98	38.74	−142.19	591.28	−14.16	−19.58	118.84	26.15	39.37	−104.21
Relativistic														
NL3	0.148	−16.24	270.70	188.80	37.34	118.30	100.50	182.60	−14.64	−20.31	136.42	25.08	73.73	29.99
TM1	0.145	−16.26	280.40	−295.40	36.84	110.60	33.55	−65.20	−14.68	−21.43	152.80	25.58	73.86	14.72
GM1	0.153	−16.32	299.70	−222.10	32.48	93.87	17.89	25.77	−14.25	−23.78	141.49	21.74	60.30	2.94
GM3	0.153	−16.32	239.90	−515.50	32.48	89.66	−6.47	55.86	−14.56	−20.79	135.45	22.07	59.46	−8.12
FSU	0.148	−16.30	229.20	−537.40	32.54	60.40	−51.41	426.60	−14.81	−19.47	140.97	25.57	47.54	−71.94
NL$\omega\rho$(025)	0.148	−16.24	270.70	188.80	32.35	61.05	−34.36	1322.00	−14.64	−20.31	136.42	25.23	50.12	−99.76
TW	0.153	−16.25	240.20	−541.00	32.76	55.30	−124.70	539.00	−14.48	−21.16	140.67	25.38	48.59	−92.51
DD-ME1	0.152	−16.23	244.50	307.60	33.06	55.42	−101.00	706.30	−14.66	−18.29	114.43	25.86	48.06	−96.35
DD-ME2	0.152	−16.14	250.90	478.30	32.30	51.24	−87.19	777.10	−14.58	−17.98	109.23	25.65	44.83	−98.43
DDHδI-25	0.153	−16.25	240.20	−540.30	25.62	48.56	81.10	928.30	−14.48	−21.16	140.70	20.23	31.73	−48.55
DDHδII-30	0.153	−16.25	240.20	−540.30	31.89	57.52	80.74	1005.00	−14.48	−21.16	140.70	25.42	38.36	−60.57
NL$\rho\delta$(2.5)	0.160	−16.05	240.40	−470.20	30.71	102.70	127.20	282.90	−13.98	−21.65	125.20	18.77	55.76	33.28
NL$\rho\delta$(1.7)	0.160	−16.05	240.40	−470.20	30.70	97.14	86.46	202.80	−13.98	−21.65	125.20	19.16	55.12	21.05
NL$\rho\delta$(0)	0.160	−16.05	240.40	−470.20	30.34	84.51	3.33	61.40	−13.98	−21.65	125.20	19.77	53.05	−4.90

B. Correlations between GLDM coefficients

The isoscalar and isovector GLDM coefficients obtained with all the nuclear models used in this paper are reported in Table I. These coefficients are intercorrelated due to common constraints that the various parametrized forces have to verify. In particular, the fitting procedure on finite-nuclei properties, for which the average density is lower than ρ_0, is likely to provide effective constraints in the density region $\rho_0 \simeq 0.1$–0.12 fm^{-3} (this point is raised, e.g., in Refs. [24,25]); as a result, the coefficients defined at ρ_0 for various effective models should show a tendency to compensate each other in order to focus the various functional predictions at lower density. To understand how a given coefficient (such as L) can affect the EOS properties away from the reference-density region, it is important to evaluate its possible connections with other coefficients. Since the equation of state of asymmetric

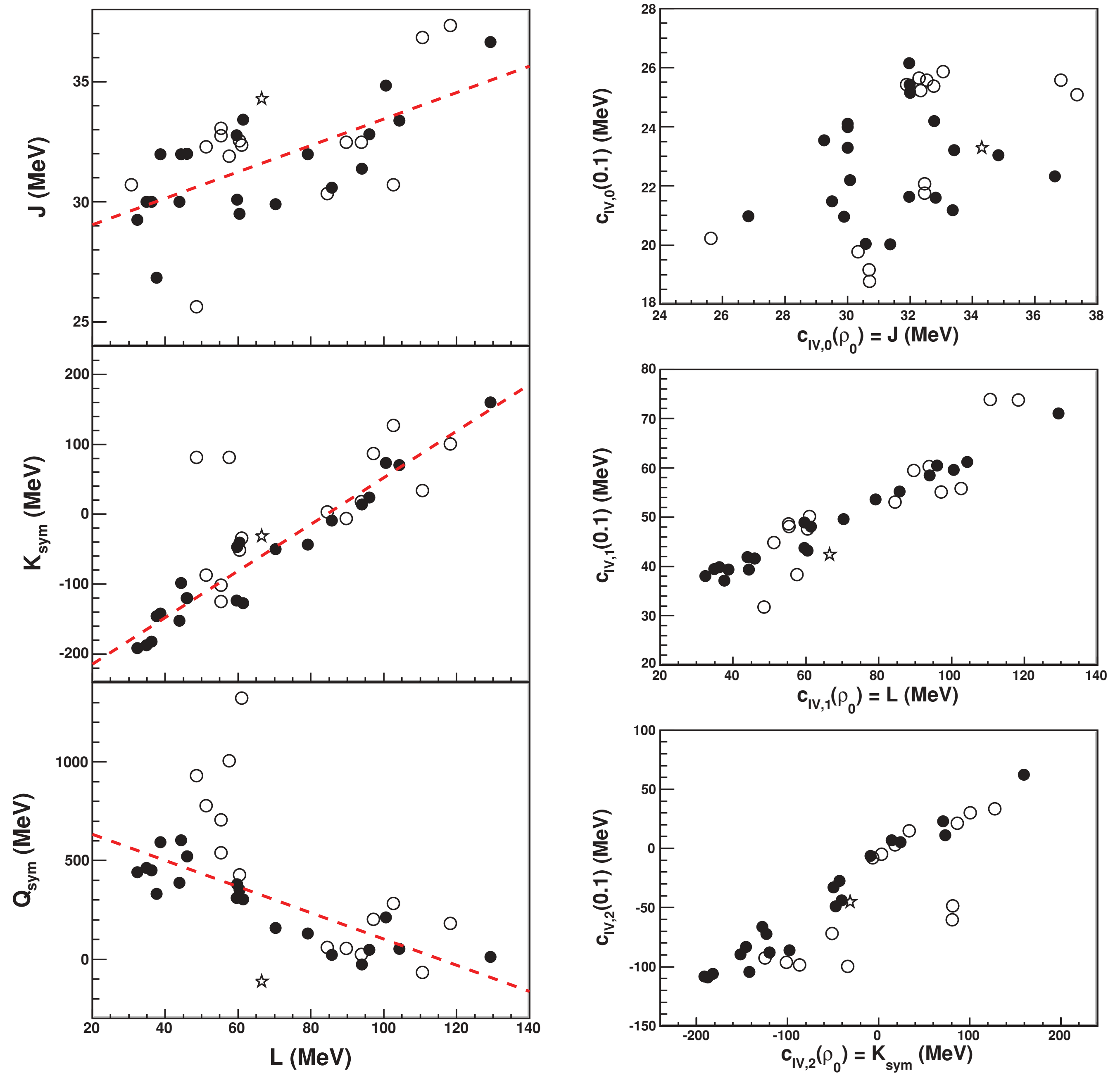

FIG. 1. (Color online) Correlations between different GLDM coefficients $c_{\mathrm{IV},n}$. Left: At saturation density, relation between L and other coefficients $c_{\mathrm{IV},n}(\rho_0)$, namely, J (top), K_{sym} (center), and Q_{sym} (bottom). Right: Relation between coefficients $c_{\mathrm{IV},n}$ defined at reference density ρ_0 or $\rho = 0.1$ fm^{-3}. Results are shown for different Skyrme models (filled symbols), relativistic models (open symbols), and BHF (star). BHF-1 is used at saturation density and BHF-2 is used at $\rho = 0.1$ fm^{-3}.

nuclear matter is our main concern here, we will concentrate on the correlations between isovector properties.

We represent in Fig. 1 different relations between GLDM isovector coefficients. On the left panel, we consider the coefficients taken at saturation density $c_{\mathrm{IV,n}}(\rho_0)$; the different plots show the correlation between L and J, K_{sym}, and Q_{sym}. As we have emphasized in Ref. [12], there is a strong L-K_{sym} correlation. The two eccentric points correspond to the relativistic models DDHδI-25 and DDHδII-30: these models include the δ meson, which is generally associated with an atypical density dependence of the symmetry energy (see, e.g., Ref. [26]). As for the symmetry energy J, it tends to increase with L, although the dispersion between different models is important. The behavior of the third-derivative coefficient Q_{sym} is less universal: a clear decreasing L-Q_{sym} correlation is obtained among the Skyrme models, but the relativistic models of lower L and the BHF point are completely out of this trend. Linear fits are represented on these plots; in the case of K_{sym} and Q_{sym}, they have been performed using only the models in agreement with the main trend.

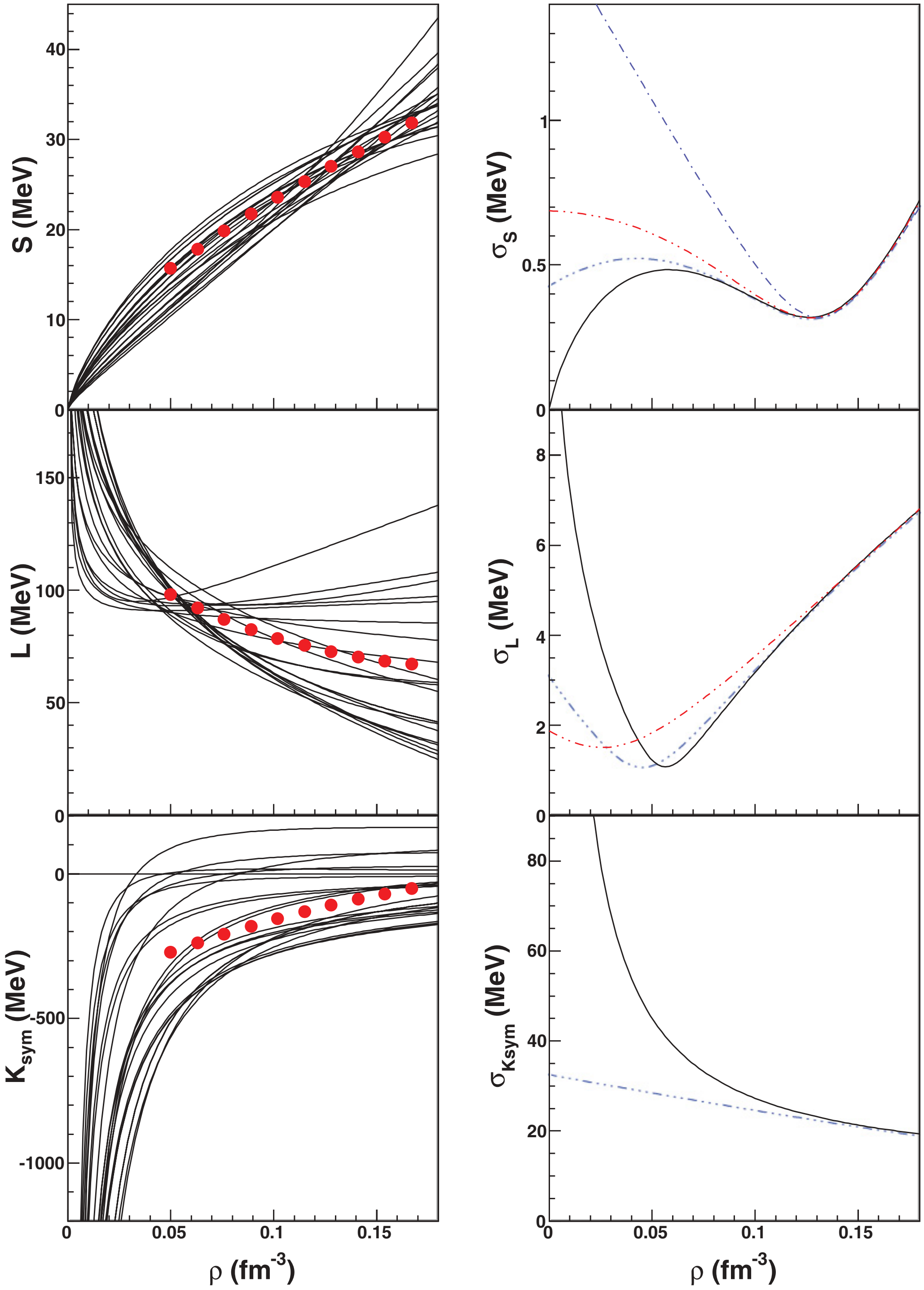

FIG. 2. (Color online) Skyrme models: Left: Symmetry-energy value (top), slope (center), and curvature (bottom) as a function of the density, calculated with complete functionals. BHF results are indicated for comparison (dots). Right: The corresponding variance for a calculation using the complete functionals (solid line) and the GLDM up to different orders: $D_1(\rho_0)$ (dotted-dashed line), $D_2(\rho_0)$ (2dotted-dashed line), and $D_3(\rho_0)$ (3dotted-dashed line).

The right panel of Fig. 1 shows the relation existing between coefficients defined at two different densities, namely, between $c_{\mathrm{IV},n}\,(\rho_0)$ and $c_{\mathrm{IV},n}$, ($\rho = 0.1$ fm^{-3}) for $n = 0$, 1, and 2. The correlations obtained in the cases of $c_{\mathrm{IV},1}$ (symmetry-energy slope) and $c_{\mathrm{IV},2}$ (symmetry-energy curvature) reflect the shape similarities between many of the density functionals. The absence of correlation in the case of $c_{\mathrm{IV},0}$ (symmetry energy) is due to the fact that $c_{\mathrm{IV},0}(0.1)$ is strongly constrained in nuclear models. This discussion is illustrated in Figs. 2 (Skyrme models) and 3 (relativistic models).

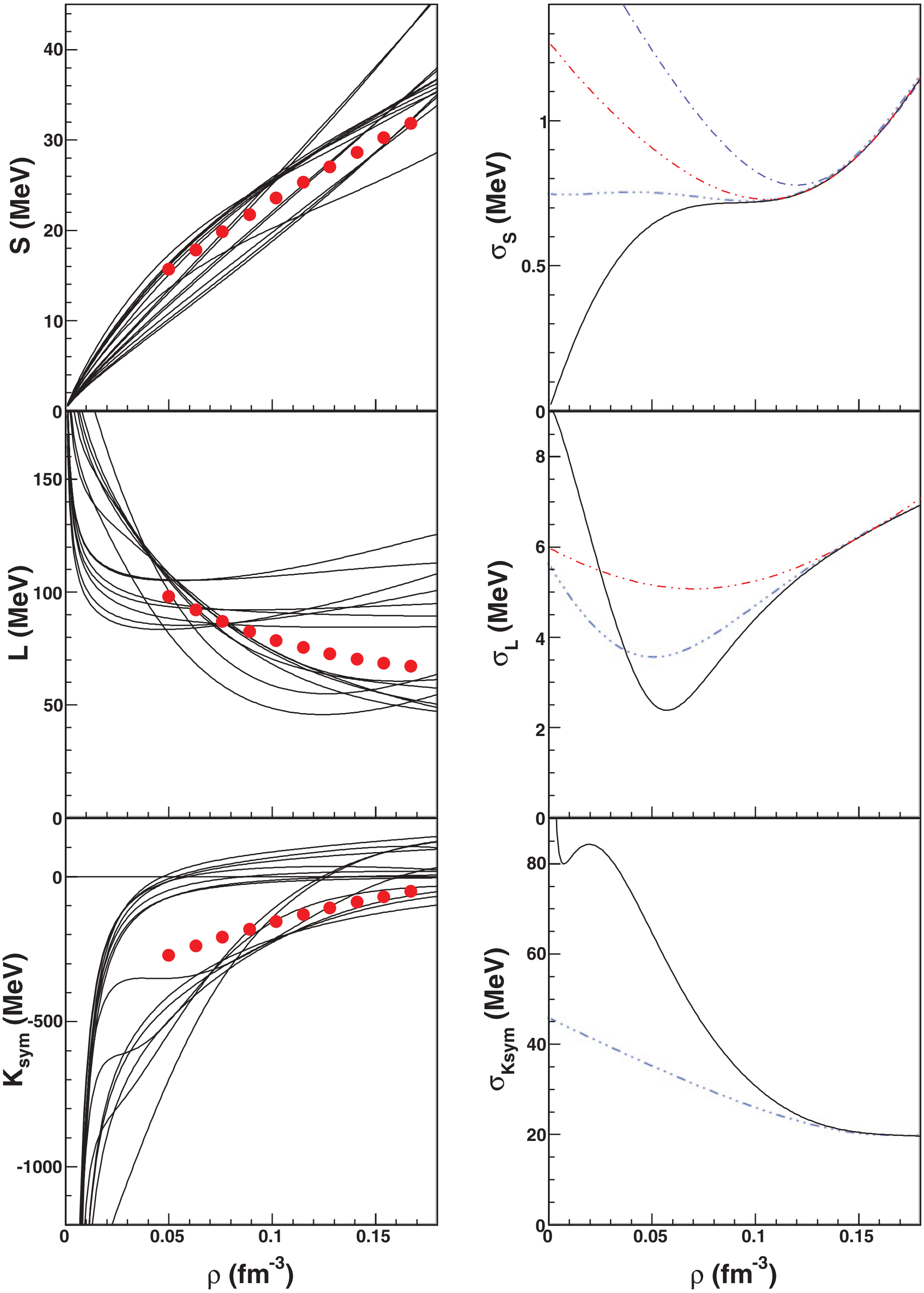

FIG. 3. (Color online) Relativistic models: Left: Symmetry-energy value (top), slope (center), and curvature (bottom) as a function of the density, calculated with complete functionals. BHF results are indicated for comparison (dots). Right: The corresponding variance for a calculation using the complete functionals (solid line) and the GLDM up to different orders: $D_1(\rho_0)$ (dotted-dashed line), $D_2(\rho_0)$ (2dotted-dashed line), and $D_3(\rho_0)$ (3dotted-dashed line).

The left panel of each figure displays the density dependence of the symmetry energy, along with its slope and curvature: $S(\rho)$, $L(\rho) = (3\rho_0)[dS/d\rho]$, and $K_{\text{sym}}(\rho) = (3\rho_0)^2[d^2S/d\rho^2]$. Note that $L(\rho)$ and $K_{\text{sym}}(\rho)$ are defined here with a constant factor involving ρ_0: they are not equivalent to the coefficients $c_{\text{IV},1}(\rho)$ and $c_{\text{IV},2}(\rho)$, except at $\rho = \rho_0$. We use here a constant factor in order to represent quantities proportional to the derivatives of $S(\rho)$. The curves are shown for all models under consideration, using the complete functionals. The comparison between Figs. 2 and 3 shows that

TABLE II. Density, proton fraction, and pressure at the thermodynamic transition (tt) and dynamic transition (td) for different nuclear models. BHF-1: Functional fit includes calculation points in the density range $\rho = [0.1; 0.35]$ fm^{-3}. BHF-2: Functional fit includes calculation points in the density range $\rho = [0.05; 0.18]$ fm^{-3}.

Model	ρ_{tt} (fm^{-3})	$Y_{p,tt}$ (MeV)	P_{tt} (fm^{-3})	ρ_{td} (fm^{-3})	$Y_{p,td}$ (MeV)	P_{td} (fm^{-3})
Microscopic						
BHF-1	0.061	0.023	0.193			
BHF-1$_{\text{para}}$	0.083	0.026	0.400			
BHF-2	0.078	0.027	0.370			
BHF-2$_{\text{para}}$	0.094	0.028	0.571			
Skyrme						
BSk14	0.090	0.033	0.483	0.081	0.030	0.381
BSk16	0.096	0.037	0.502	0.087	0.035	0.402
BSk17	0.095	0.036	0.499	0.086	0.034	0.397
G_σ	0.063	0.013	0.278	0.054	0.010	0.172
R_σ	0.067	0.014	0.312	0.058	0.012	0.202
LNS	0.088	0.031	0.614	0.077	0.028	0.469
NRAPR	0.083	0.034	0.545	0.073	0.030	0.413
RATP	0.097	0.037	0.500	0.086	0.034	0.390
SV	0.071	0.021	0.372	0.061	0.016	0.235
SGII	0.086	0.026	0.401	0.077	0.024	0.311
SkI2	0.064	0.014	0.291	0.054	0.011	0.170
SkI3	0.071	0.022	0.363	0.062	0.018	0.244
SkI4	0.081	0.024	0.332	0.072	0.021	0.234
SkI5	0.061	0.014	0.271	0.051	0.010	0.149
SkI6	0.082	0.026	0.352	0.073	0.024	0.257
SkMP	0.072	0.020	0.357	0.062	0.017	0.241
SkO	0.073	0.020	0.413	0.062	0.017	0.270
Sly230a	0.090	0.039	0.404	0.081	0.037	0.319
Sly230b	0.089	0.038	0.462	0.080	0.036	0.362
SLy4	0.089	0.038	0.461	0.080	0.036	0.361
SLy10	0.091	0.042	0.447	0.083	0.041	0.369
Relativistic						
NL3	0.065	0.021	0.422	0.054	0.016	0.236
TM1	0.070	0.025	0.511	0.060	0.020	0.324
GM1	0.074	0.019	0.408	0.067	0.016	0.290
GM3	0.069	0.018	0.356	0.063	0.016	0.267
FSU	0.082	0.037	0.487	0.074	0.035	0.385
NL$\omega\rho$(025)	0.089	0.038	0.689	0.080	0.034	0.530
TW	0.084	0.037	0.544	0.075	0.033	0.384
DD-ME1	0.085	0.038	0.605	0.070	0.033	0.404
DD-ME2	0.087	0.039	0.594	0.072	0.034	0.409
DDHδI-25	0.085	0.022	0.144	0.079	0.021	0.100
DDHδII-30	0.086	0.038	0.285	0.080	0.037	0.231
NL$\rho\delta$(2.5)	0.062	0.009	0.173	0.057	0.008	0.116
NL$\rho\delta$(1.7)	0.064	0.011	0.197	0.059	0.009	0.143
NL$\rho\delta$(0)	0.069	0.014	0.276	0.063	0.012	0.197

the relativistic models present more variability in the shape of the density functional than Skyrme models, as we have shown in Ref. [26]. This comes from the different ways of describing the nuclear interaction by meson exchange in the effective relativistic framework; in particular, the inclusion of the δ meson has a strong effect on the density dependence of L. We can also notice that relativistic models such as GM1 and GM3, which were built for astrophysical purposes, have not been explicitly fitted on laboratory data.

Considering globally the Skyrme and relativistic functionals, we can notice two common convergence regions. One concerns the symmetry energy: all curves tend to cross around the density $\rho \simeq 0.11$ fm^{-3}, taking values $S(0.11 \text{ fm}^{-3}) = 24 \pm 4$ MeV. This behavior was expected, following the previous remark that finite nuclei provide fitting constraints at density slightly below saturation; similar observations have been made, e.g., in Ref. [27]. The second convergence region concerns the symmetry-energy slope $L(\rho)$: the different curves show a marked tendency to cross at about $\rho_0/3$. In contrast, no convergence effect appears for the second derivative $K_{\text{sym}}(\rho)$.

On the right panel of Figs. 2 and 3, we represent the density dependence of the variance between the values taken by different models. Denoting $X(\rho) = \{S(\rho), L(\rho), K_{\text{sym}}(\rho)\}$, the variance is given by

$$\sigma_X(\rho) = \sum_i \sqrt{[X_i(\rho) - \bar{X}(\rho)]^2}\ , \quad \bar{X}(\rho) = \frac{1}{N}\sum_{i=1}^{N} X_i(\rho), \tag{8}$$

where the index i runs over the N models considered. The convergent trends are reflected by the density dependence of the respective variances. In the case of Skyrme functionals, a clear minimum of σ_S occurs at $\rho \simeq 0.13$ fm^{-3}. With relativistic models, we observe a plateau around an inflexion point at $\rho \simeq 0.1$ fm^{-3}. Note that σ_S is constrained to cancel at zero density; in such a condition, the inflexion point can be considered as a criterion of convergent trend. The convergence effect is even more clear in the case of the symmetry-energy slope $L(\rho)$; both Skyrme and relativistic models present a sharp minimum of σ_L at $\rho \simeq 0.06$ fm^{-3}.

These results indicate that the correlations existing between J, L, K_{sym}, and Q_{sym} may be associated with effective constraints on the values of $S(\rho \simeq 0.12\,\text{fm}^{-3})$ and $L(\rho \simeq 0.06\,\text{fm}^{-3})$. To verify this, we show on the same figures the variances obtained when the curves $X(\rho)$ are calculated using the GLDM at different orders, with reference density ρ_0. A minimum of σ_S in the density range 0.11–0.13 fm^{-3} is obtained with versions $D_1(\rho_0)$ and $D_2(\rho_0)$ of the GLDM. The version $D_3(\rho_0)$ gives a clear minimum of σ_L at $\rho \simeq 0.05$ fm^{-3}. We can conclude that the correlations between the GLDM coefficients are related with convergence effects for $S(\rho)$ and $L(\rho)$ in the subsaturation density region.

Let us remark that the convergence of the L values at $\rho \simeq 0.06$ fm^{-3} is easily interpreted as a geometrical consequence of a constraint on $S(\rho \simeq 0.12$ fm$^{-3})$. Indeed, let us imagine a constraint fixing the values (ρ_c, E_c) such that all models have to verify $S(\rho_c) = E_c$. Since we also have the condition $S(0) = 0$, it turns out that, for all models, $L(\rho)$ takes the value $L_c = E_c \times 3\rho_0/\rho_c$ at least once on the interval $[0, \rho_c]$. For instance, if $\rho_c = 0.12$ fm^{-3}, $E_c = 25$ MeV, and $\rho_0 = 0.16$ fm^{-3}, we have $L_c = 100$ MeV.

C. Comparison between GLDM and complete functionals

We now explore the accuracy of the GLDM approximation on reproducing the core-crust transition obtained with the

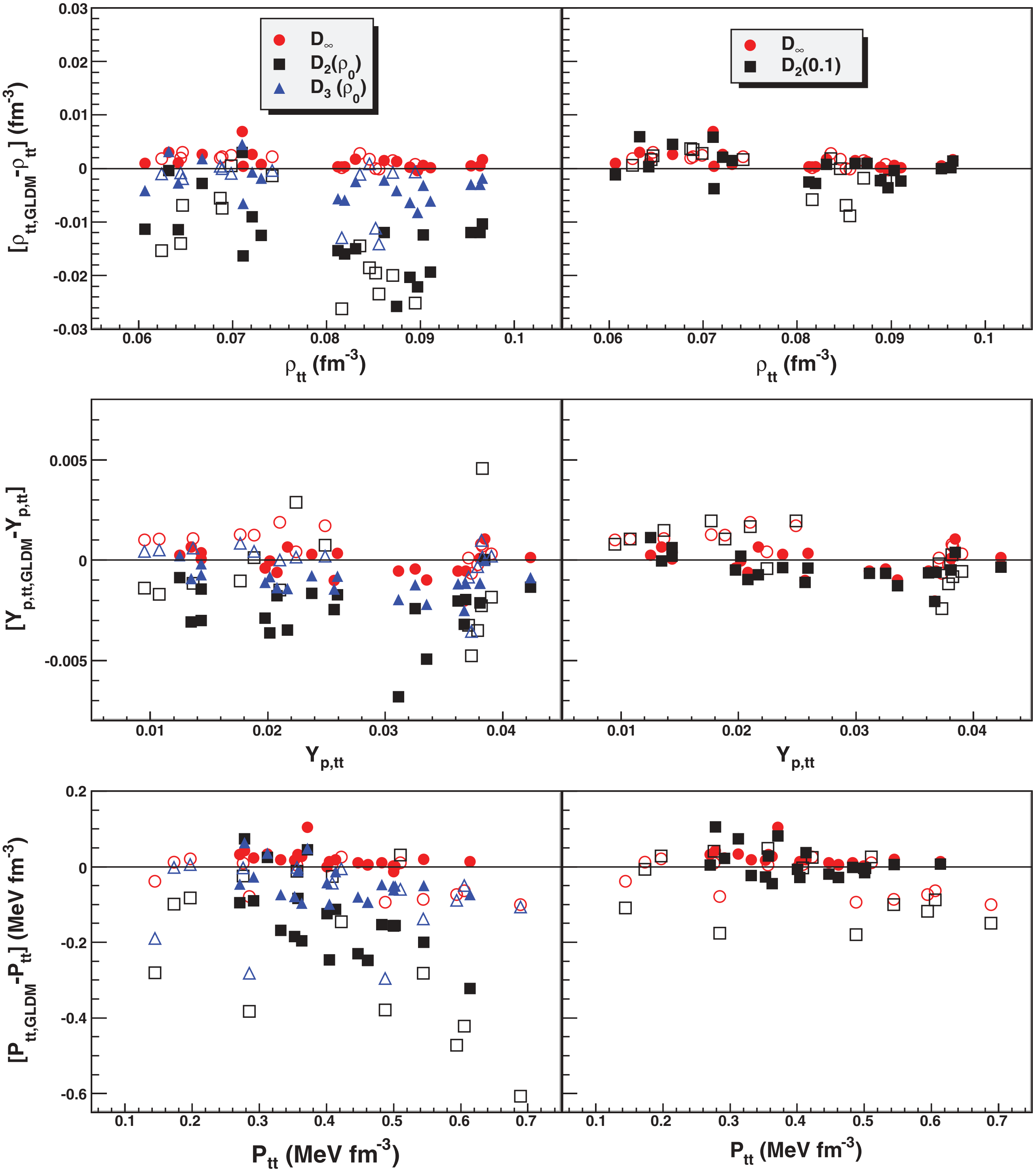

FIG. 4. (Color online) Predictive power of the GLDM development. For different Skyrme and relativistic models, we compare the values of ρ_{tt} (top), $Y_{p,tt}$ (center), and P_{tt} (bottom) versus L, calculated with the complete functionals and with several versions of the corresponding GLDM (see text). Left: D_∞, second-, and third-order development around saturation density [$D_{2,3}(\rho_0)$]. Right: D_∞ and second-order development around $\rho = 0.1$ fm^{-3} [$D_2(0.1)$].

complete model on which it has been built. This procedure allows us to estimate whether the core-crust transition can be efficiently characterized by a limited set of EOS properties determined at a fixed density.

The discussion of the core-crust transition is performed in the thermodynamic framework, which means that, for simplicity, the transition is defined as the crossing between β equilibrium and the thermodynamic spinodal border. The corresponding transition density, proton fraction, and pressure are denoted, respectively, ρ_{tt}, $Y_{p,tt}$, and P_{tt}, where the index tt stands for *thermodynamic transition*. In Sec. IV, we will also discuss the *dynamic transition* defined using the finite-size spinodal border, in which case the index td will be used. The transition properties in both thermodynamic and dynamic cases are given in Table II.

We compare in Fig. 4 the transition properties (ρ_{tt}, $Y_{p,tt}$, and P_{tt}) obtained with the complete functionals and different versions of their associated GLDMs. On the left panel, we consider second- and third-order developments around saturation density, namely, $D_2(\rho_0)$ and $D_3(\rho_0)$; on the right panel, we consider the second-order development around a lower reference density $\rho_{\mathrm{ref}} = 0.01\ \mathrm{fm}^{-3}$, namely, $D_2(0.1)$. On each part, we add the results from the fully developed GLDM, D_∞, for which the only difference with the complete functional is due to extra-parabolic terms in the nuclear interaction. For the BHF model, the functional is equivalent by construction to its associated D_∞ model.

We can see that $D_2(\rho_0)$ leads generally to an important underestimation of ρ_{tt}, $Y_{p,tt}$, and P_{tt}. This means that, in a development around saturation density, terms beyond order 2 (i.e., beyond K_{sym}) have a large impact on the properties of the core-crust transition; the correlations observed between L and these properties can occur only if higher-order corrections are either correlated with L, or similar, for most of the functionals. The underestimation is strongly attenuated, but still present, with $D_3(\rho_0)$, which involves the knowledge of isovector coefficients until Q_{sym}. The situation is much improved if we use a development around $\rho_{\mathrm{ref}} = 0.1\ \mathrm{fm}^{-3}$. The accuracy is globally better with $D_2(0.1)$ than with $D_3(\rho_0)$; furthermore, it is nearly as good with $D_2(0.1)$ as with D_∞, which means that, at $\rho_{\mathrm{ref}} = 0.1\ \mathrm{fm}^{-3}$, it is enough to perform the development up to second order. It is then important to relate experimental observables with the symmetry-energy density dependence directly in this low-density region. This is also appropriate since the nucleus properties used to constrain the symmetry energy are often associated with subsaturation densities (neutron-skin thickness, resonances, multifragmentation, isospin diffusion, ...).

Let us note that effective nuclear models have an important role to play for the fine-tuning of the curvature properties of the EOS, crucial for the prediction of the core-crust transition. Indeed, although microscopic methods such as BHF are necessary to obtain reliable EOS values far away from the phenomenological constraints (in particular, for neutron matter and at high density), they can not be used as a reference for the EOS curvature. The numerical BHF results for $E(\rho)$ do not allow the direct determination of second derivatives; the EOS has to be fitted (see, for instance, Ref. [28]), and the resulting curvature properties are sensitive to the fitting conditions. We show in Fig. 5 how this affects the predictions for the core-crust transition. This figure displays the values of ρ_{tt}, $Y_{p,tt}$, and P_{tt} obtained by using the BHF calculations in different ways. In the first version, BHF-1, the fit is performed on the density interval $\rho = [0.1; 0.35]\ \mathrm{fm}^{-3}$: this is the version that is used to establish the GLDM coefficients at ρ_0. In order to focus on the subsaturation region, we have considered a second version, BHF-2, for which the fit is performed on the density interval $\rho = [0.05; 0.18]\ \mathrm{fm}^{-3}$: this is the version we will use afterward to define the BHF core-crust transition. For now, let us compare the BHF-1 and BHF-2 predictions. The GLDM coefficients at $\rho_{\mathrm{ref}} = 0.1\ \mathrm{fm}^{-3}$ have been determined for both versions, and there are significant differences in the transition properties predicted by the $D_2(0.1)$ expansion in each case. A similar contrast appears between the results obtained with the full BHF-1 and BHF-2 EOS. In addition to these two versions of BHF calculations, the figure also shows the complete and GLDM results for the Skyrme force LNS [47], the fitting procedure of which involves the BHF equation of state. From the span of results we obtain, it is clear that a microscopic calculation does not lead to a unique prediction for the core-crust transition properties; phenomenological constraints

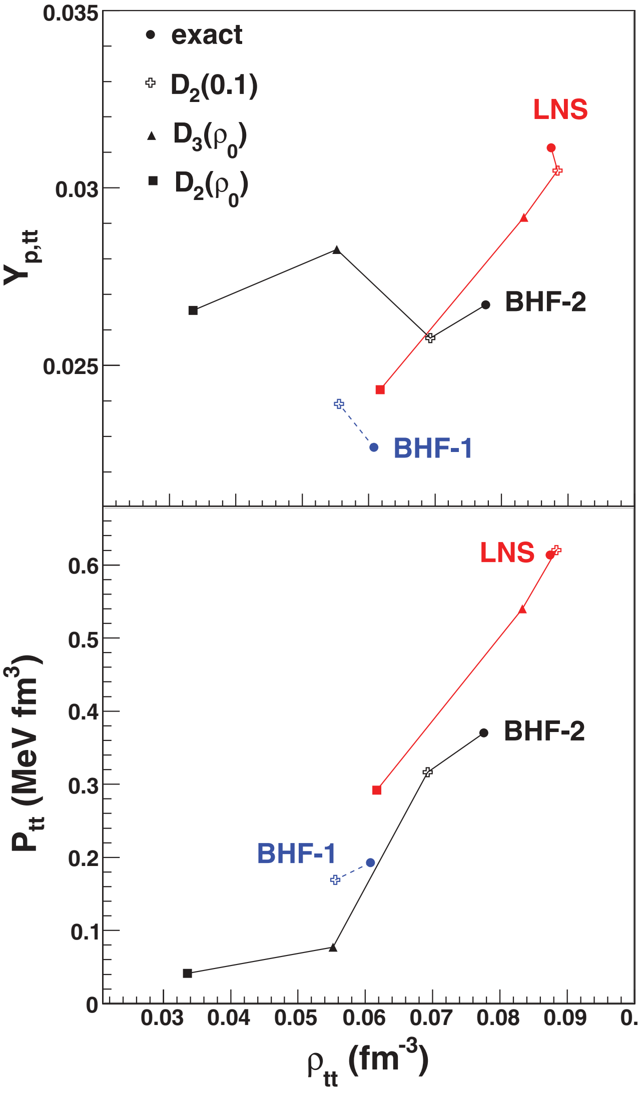

FIG. 5. (Color online) Comparison between exact and GLDM versions of three functionals based on BHF calculations: LNS [47] (Skyrme-type force including constraints from BHF), BHF-1 (fit of the BHF EOS including densities in the range $\rho = [0.1; 0.35]\ \mathrm{fm}^{-3}$), and BHF-2 (fit of the BHF EOS including lower densities in the range $\rho = [0.05; 0.18]\ \mathrm{fm}^{-3}$).

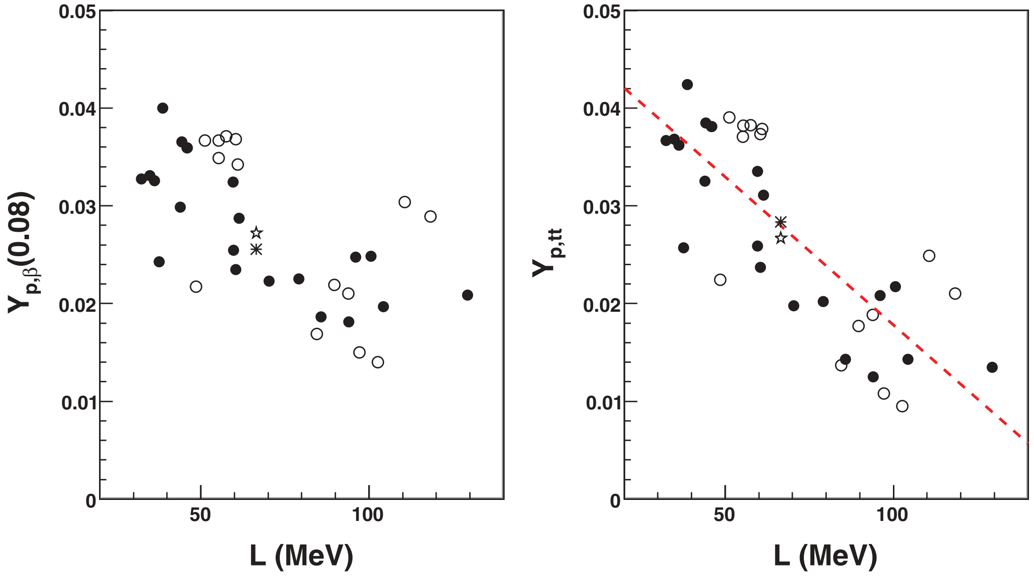

FIG. 6. (Color online) Effect of L on the proton fraction at β equilibrium for a fixed density $\rho = 0.08$ fm^{-3} (left) and at thermodynamic spinodal crossing (right) for different nuclear models: Skyrme (filled symbols), relativistic (open symbols), BHF-2 (star), and BHF-2$_{\text{para}}$ (asterisk).

from finite nuclei will be essential to improve our knowledge of the low-density EOS.

III. CORRELATION BETWEEN *L* AND THE CORE-CRUST TRANSITION POINT

We consider in this section the specific role of the symmetry-energy slope L in the determination of the core-crust transition, defined here as the crossing between the line of β equilibrium and the thermodynamic spinodal contour. We summarize the study performed in Ref. [12], and present more details that support this previous analysis.

A. Position of the transition point

The most direct impact of the symmetry energy on neutron-star structure concerns the proton fraction $Y_p(\rho)$ in stellar matter, which is fixed by β equilibrium. For a given density, a lower symmetry energy corresponds to a lower proton fraction. Thus, as far as a high value of L can be correlated with a low value of the symmetry energy at subsaturation, we expect

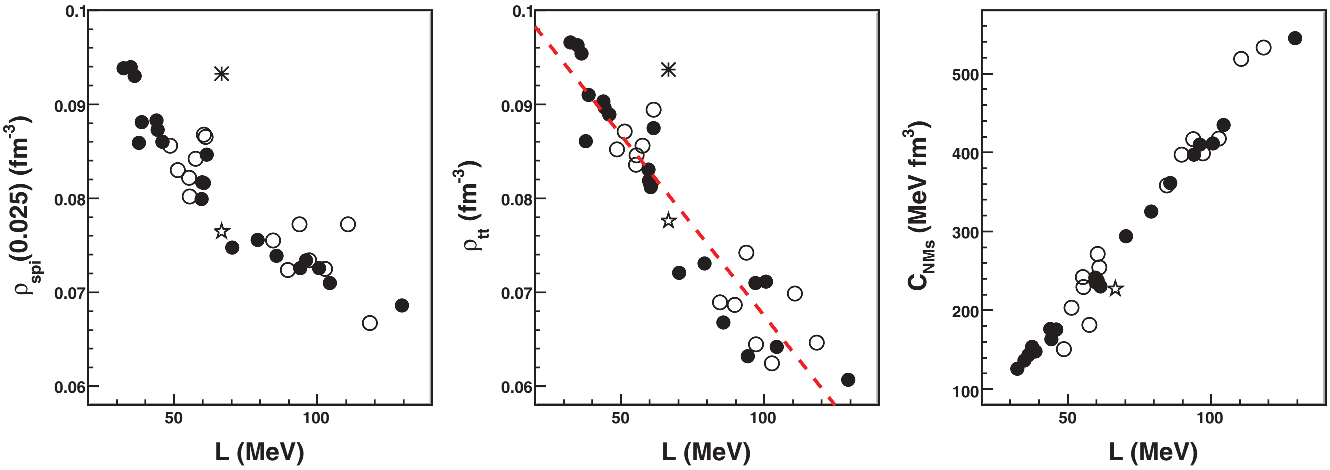

FIG. 7. (Color online) Effect of L on the density at thermodynamic spinodal border for a fixed proton fraction $Y_p = 0.025$ (left) and at β equilibrium (center). Right: Correspondence between L and the energy-density curvature of neutron matter at symmetric spinodal density $C_{\text{NM},s}$ (see text). Results are shown for different nuclear models: Skyrme (filled symbols), relativistic (open symbols), BHF-2 (star), and BHF-2$_{\text{para}}$ (asterisk) (both BHF results are identical for neutron matter).

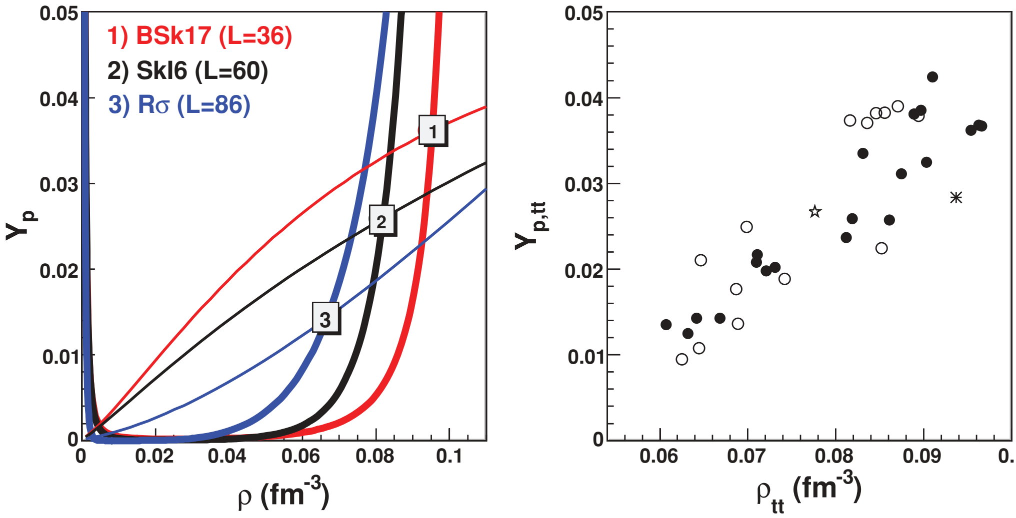

FIG. 8. (Color online) Simultaneous effect of L on the proton fraction at β equilibrium and on the thermodynamic spinodal border of neutron-rich matter. Left: Spinodal contours and β equilibrium for three Skyrme models: BSk17 ($L = 36$ MeV), SkI6 ($L = 60$ MeV), and R_σ ($L = 86$ MeV). Right: Correlation between ρ_{tt} and $Y_{p,tt}$ for different nuclear models: Skyrme (filled symbols), relativistic (open symbols), BHF-2 (star), and BHF-2_{para} (asterisk).

higher-L models to provide lower values of $Y_{p,tt}$. This point is illustrated by Fig. 6. At fixed density $\rho = 0.08$ fm^{-3}, for increasing L, the β-equilibrium proton fraction decreases. This trend is confirmed and even accentuated if, instead of fixing the density, we consider the proton fraction at the transition point. The dispersion observed in both cases is essentially due to different values of the symmetry energy at saturation density, as will be discussed in the following.

Let us now consider the impact of L on the transition density ρ_{tt}, illustrated by Fig. 7. The correlation between L and ρ_{tt} is a well-known feature [9]; however, its explanation is less intuitive than in the case of the L-$Y_{p,tt}$ correlation. Furthermore, it can not be explained just as a consequence of the behavior of $Y_{p,tt}$, as we see on the left panel of the figure; even for a fixed proton fraction $Y_p = 0.025$, the spinodal border shows a clear decreasing correlation with L. This feature can be understood as a consequence of the strong link existing between L and the energy-density curvature of neutron matter taken at symmetric spinodal density ρ_s:

$$C_{\text{NM},s} = \frac{2}{3\rho_0}L + \frac{1}{3\rho_0}\sum_{n\geqslant 2} c_{\text{IV},n}\frac{x_s^{n-2}}{(n-2)!}\left[\frac{n+1}{n-1}x_s + \frac{1}{3}\right] + \frac{\partial^2\left[\rho\left(E_{\text{kin}} - E_{\text{kin}}^{\text{para}}\right)\right]}{\partial\rho^2} \tag{9}$$

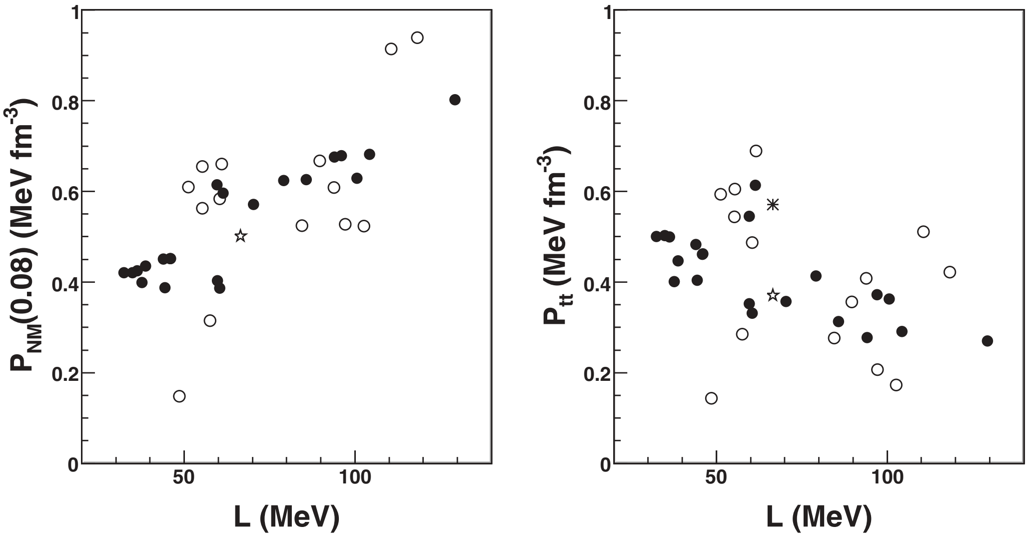

FIG. 9. Impact of L on the pressure of neutron-rich matter at subsaturation density for different nuclear models: Skyrme (filled symbols), relativistic (open symbols), BHF-2 (star), and BHF-2_{para} (asterisk). Both BHF-2 results are identical for neutron matter. Left: Pressure of pure neutron matter for a fixed density typical of the transition $\rho = 0.08$ fm^{-3}. Right: Thermodynamic transition pressure.

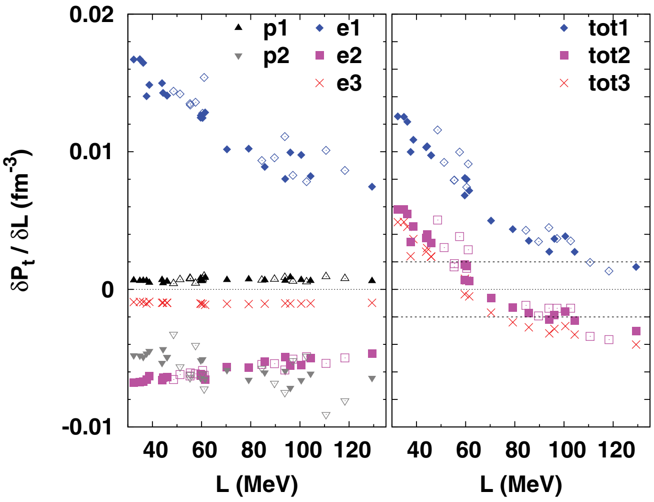

FIG. 10. (Color online) Estimation of different contributions to the variation of P_{tt} with L (see text). Left: Separated contributions due to the transition position shift (indices $p1$ and $p2$) and to the variation of the GLDM coefficients $c_{\mathrm{IV},n}$ in the expression of P (indices $e1$, $e2$, and $e3$ for $n = 1$, 2, and 3 respectively). Right: Sum of the contributions, considering the contribution of $\delta c_{\mathrm{IV,n}}/\delta L$ up to order $n = 1, 2$ and 3 (respective indices: tot1, tot2, and tot3). The horizontal lines indicate the region where the pressure variation is compatible with zero within the estimated uncertainty. Filled symbols: Skyrme models; open symbols: relativistic models.

with $x_s = (\rho_s - \rho_0)/(3\rho_0)$. Since all models yield a symmetric spinodal density close to 0.1 fm^{-3}, so that $x_s \simeq -1/9$, the term $n = 2$ is nearly canceled; this reinforces the dominance of L in the determination of $C_{\mathrm{NM,s}}$.

Figure 8 illustrates how L affects independently the proton fraction at β equilibrium and the spinodal contour in the neutron-rich region. Due to the typical geometry of these respective lines, the two effects reinforce each other, leading to a robust correlation between L, ρ_{tt}, and $Y_{p,tt}$.

B. Pressure at the transition point

The link between L and the core-crust transition pressure P_{tt} is more problematic. In order to make this link explicit, let us write the pressure in the GLDM framework

$$P(\rho, y) = \frac{\rho^2}{3\rho_0}\left[Ly^2 + \sum_{n\geqslant 2}(c_{\mathrm{IS},n} + c_{\mathrm{IV},n}y^2)\frac{x^{n-1}}{(n-1)!}\right] + \rho^2\frac{\partial\left(E_{\mathrm{kin}} - E^{\mathrm{para}}_{\mathrm{kin}}\right)}{\partial\rho}. \tag{10}$$

From this expression, we expect that, for a given density, the pressure of neutron-rich matter should increase with L, which is the leading coefficient. This trend appears on the left panel of Fig. 9, representing the relation between L and the pressure of pure neutron matter P_{NM} at $\rho = 0.08$ fm^{-3}. Thus, a positive correlation between L and P_{tt} should be obtained if we could neglect the density shift due to the L-ρ_{tt} correlation, as well as the effect of higher-order coefficients. However, as can be seen on the right panel of the figure, the results for $P_{tt}(L)$ present an important dispersion and we can not extract a clear correlation, although a decreasing trend can be observed among Skyrme models. Four eccentric points close to $L = 60$ MeV weaken this correlation between Skyrme models: they correspond to atypical relations between L and K_{sym}, which also affect the plot $P_{\mathrm{NM}}(0.08$ fm$^{-3})$.

The lack of correlation between L and P_{tt} when independent models are considered results from a delicate balance between opposite effects, as we have discussed in Ref. [12]. This is shown by separating the different

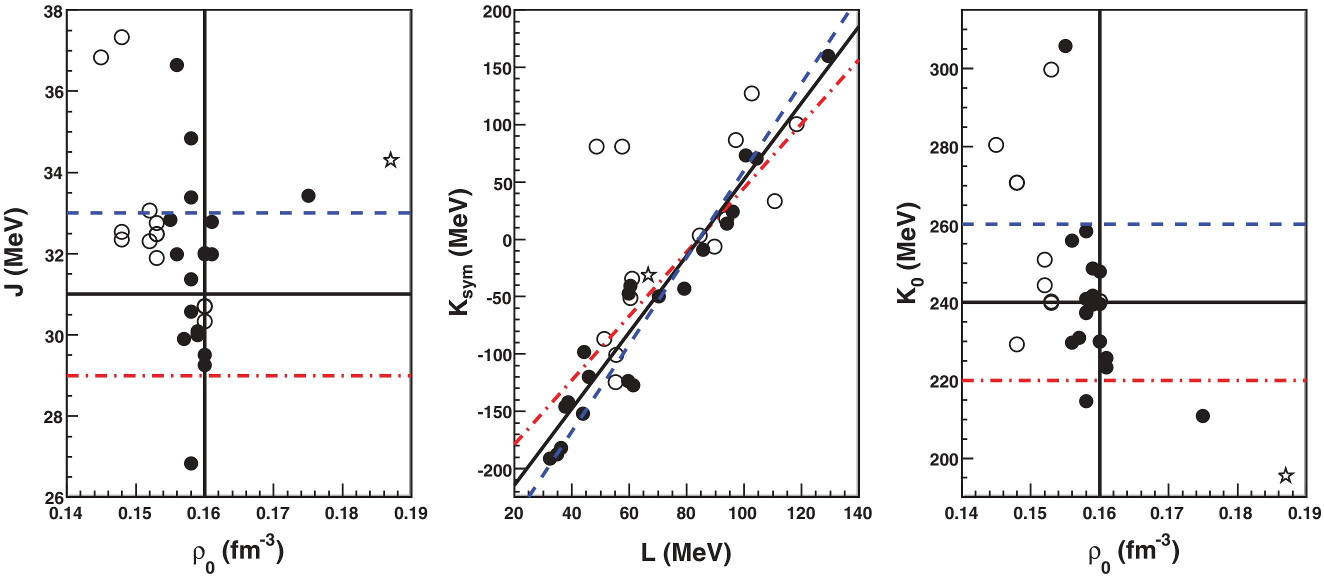

FIG. 11. (Color online) Typical variation for the values of J, $K_{\mathrm{sym}}(L)$, and K_0. We represent these quantities for different Skyrme models (filled symbols), relativistic models (open symbols), and BHF-1 (star). The lines show the different values that are used for the standard schematic model (see text).

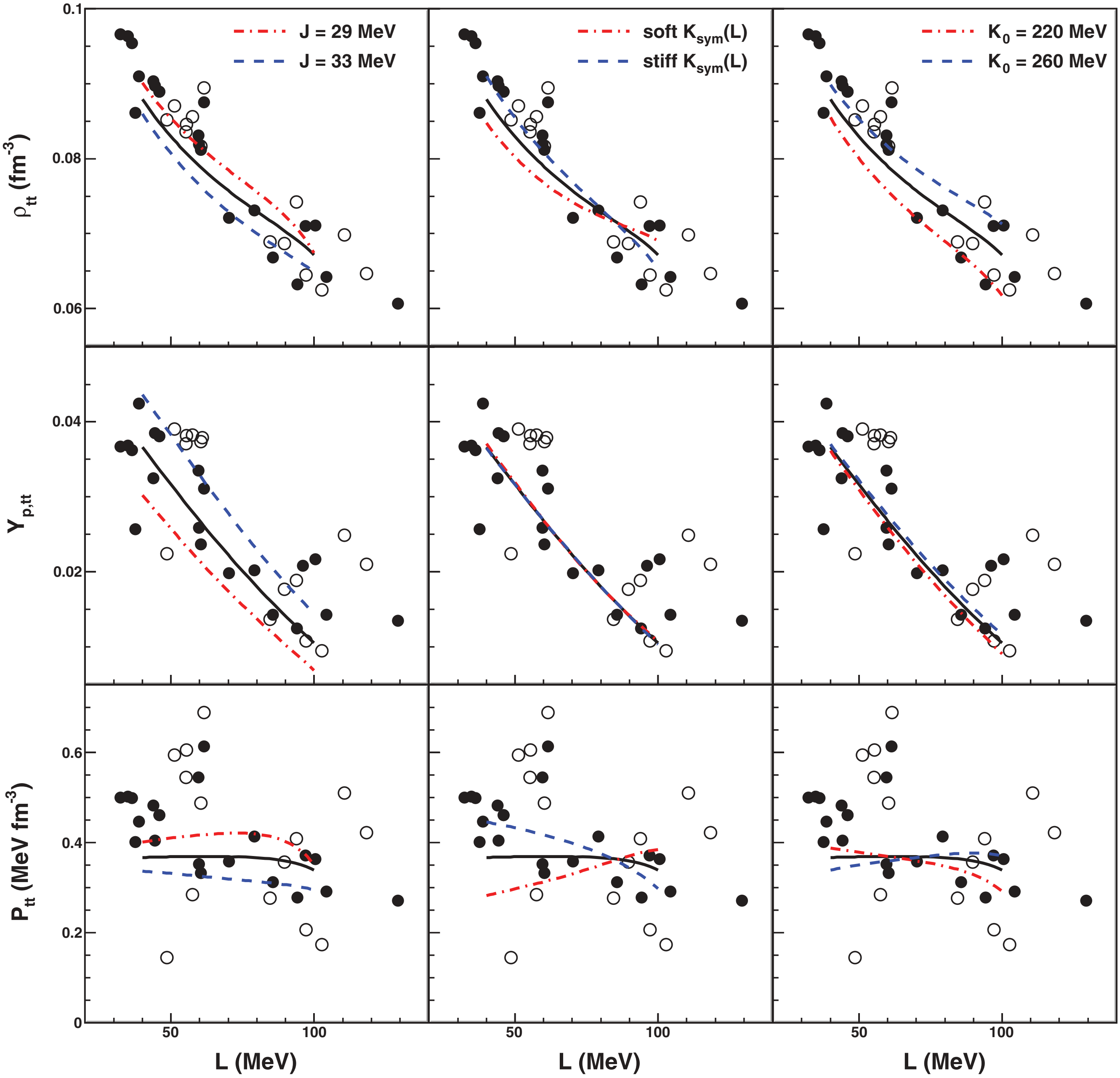

FIG. 12. (Color online) Predictions of the standard schematic model for the transition density, proton fraction, and pressure, compared with complete effective models: Skyrme (filled symbols) and relativistic (open symbols) models. Left: Varying the symmetry energy at saturation J. Center: Varying the relation $K_{\mathrm{sym}}(L)$. Right: Varying the incompressibility at saturation K_0.

contributions we can estimate from the GLDM formula. We distinguish two kinds of contributions to the variation dP_{tt}/dL: (i) variations occurring at a fixed density (ρ, y), resulting only from the modifications of the coefficients in Eq. (10), which defines $P(\rho, y)$; and (ii) variations due to a shift $(\delta\rho, \delta y)$ for a fixed expression of $P(\rho, y)$, i.e. frozen values of the coefficients in Eq. (10). The contributions of the first kind come from the explicit L dependence of Eq. (10), and from correlations between L and higher-order coefficients $c_{\mathrm{IV,n}}$. In practice, we will consider the following terms:

$$\left[\frac{\delta P_{tt}}{\delta L}\right]_{e1} = \frac{\partial P}{\partial L}(\rho_{tt}, y_{tt}), \tag{11}$$

$$\left[\frac{\delta P_{tt}}{\delta L}\right]_{e2} = \frac{\partial P}{\partial K_{\mathrm{sym}}}(\rho_{tt}, y_{tt})\frac{\delta K_{\mathrm{sym}}}{\delta L}, \tag{12}$$

$$\left[\frac{\delta P_{tt}}{\delta L}\right]_{e3} = \frac{\partial P}{\partial Q_s}(\rho_{tt}, y_{tt})\frac{\delta Q_s}{\delta L}, \tag{13}$$

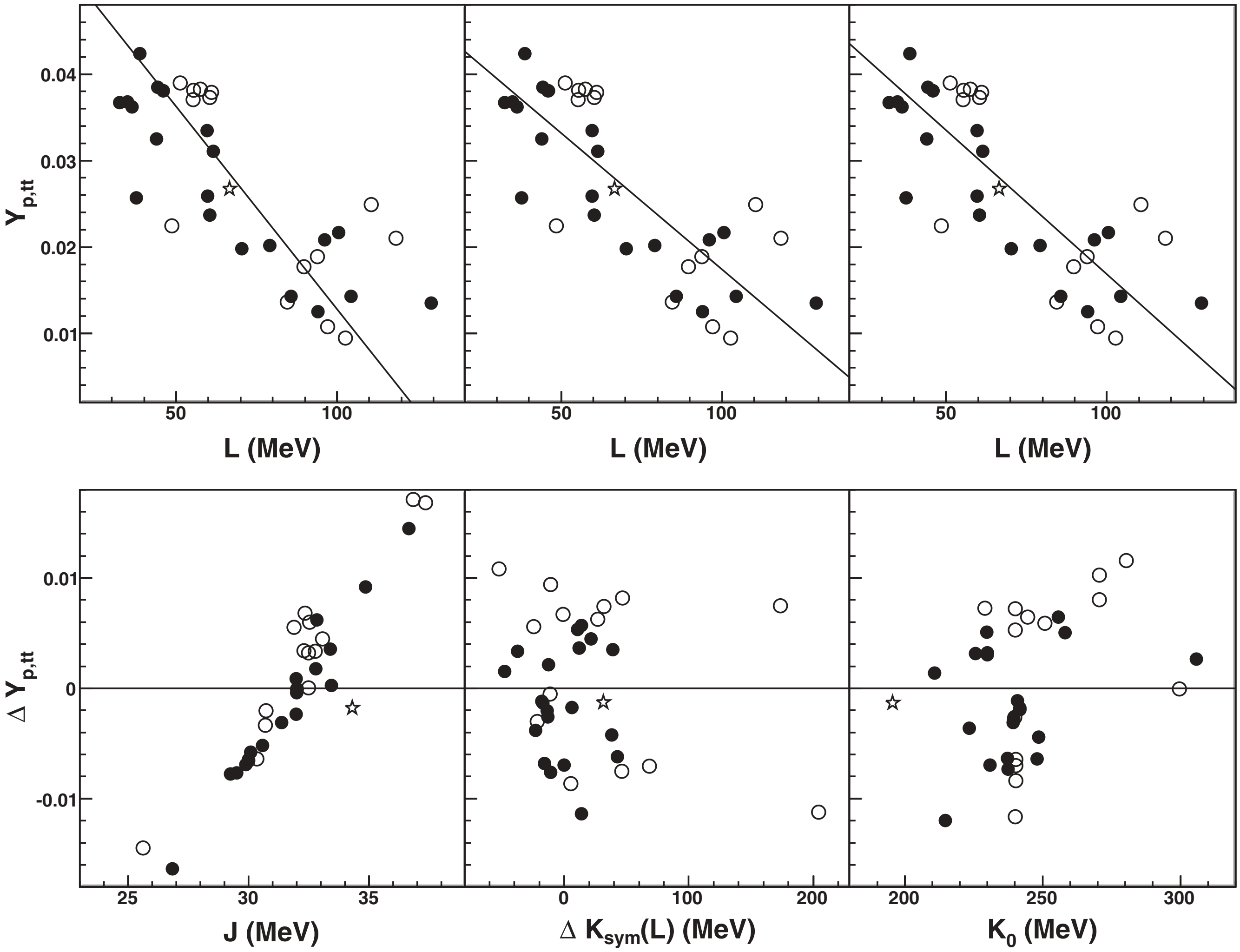

FIG. 13. Relation between the dispersion of $Y_{p,tt}(L)$ and the dispersion of GLDM properties [J, K_0, $\Delta K_{\rm sym}(L)$] associated with the different models (see text). Nuclear models: Skyrme (filled symbols), relativistic (open symbols), and BHF-2 (star).

where the index e means that the modification concerns the *expression* of the pressure, and the number gives the order of the modified coefficient. The contributions of the second kind, resulting from the density *position* of the transition point, are characterized by the index p. We distinguish the respective effects of total density and asymmetry:

$$\left[\frac{\delta P_{tt}}{\delta L}\right]_{p1} = \frac{\partial P}{\partial \rho}(\rho_{tt}, y_{tt})\frac{\delta \rho_{tt}}{\delta L}, \qquad (14)$$

$$\left[\frac{\delta P_{tt}}{\delta L}\right]_{p2} = \frac{\partial P}{\partial y}(\rho_{tt}, y_{tt})\frac{\delta y_{tt}}{\delta L}. \qquad (15)$$

The variations of the quantities depending on L are fixed empirically using as a reference the correlations that are observed between different models. From linear fits, we extract $\delta\rho_{tt}/\delta L = -3.84 \times 10^{-4}$ MeV^{-1} fm^{-3}, $\delta y_{tt}/\delta L = 6.08 \times 10^{-4}$ MeV^{-1}, $\delta K_{\rm sym}/\delta L = 3.33$, and $\delta Q_s/\delta L = -6.63$. Note that, in the case of Q_s, the correlation with L is observed only within the Skyrme models, which are used to perform the linear fit.

These various contributions are represented in Fig. 10. It appears that the contribution of the asymmetry shift is quite marginal, and the overall $\delta P_{tt}/\delta L$ essentially results from the balance between three terms: $[\delta P_{tt}/\delta L]_{e1}$, which is large and positive, is compensated by the conjugated effect of $[\delta P_{tt}/\delta L]_{e2}$ and $[\delta P_{tt}/\delta L]_{p1}$. These two negative contributions, $e2$ and $p1$, are of the same order of magnitude; this means that the correlation L-$K_{\rm sym}$ has the same importance as the correlation L-ρ_{tt} in explaining why we do not observe an increasing correlation $P_{tt}(L)$.

In addition, we can see that the term $(\delta P_{tt})/\delta L)_{e3}$ due to the L-$Q_{\rm sym}$ relation brings an additional negative contribution, but of much lower magnitude than the term $e2$. This result means that, although the third-order term of the GLDM has a strong impact on the absolute value of P_{tt} (as it was observed in Fig. 4), the L-$Q_{\rm sym}$ correlation is not crucial in the determination of $\delta P_{tt}/\delta L$; in other words, the third-order correction does not depend strongly on L. On the other hand, let us note that the strong dispersion of $Q_{\rm sym}$ values in the case of relativistic models is bound to cause a strong dispersion in $P_{tt}(L)$.

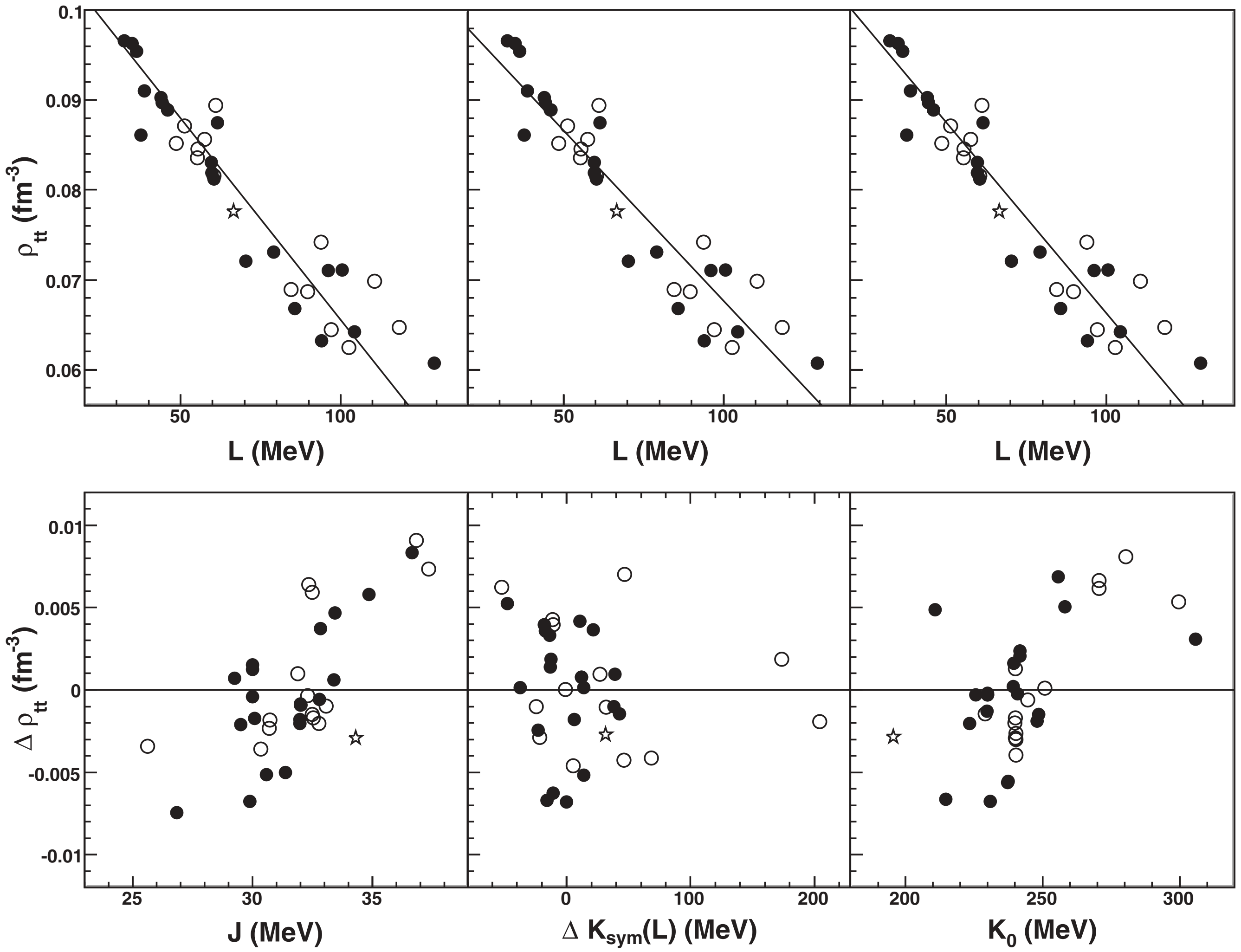

FIG. 14. Relation between the dispersion of $\rho_{tt}(L)$ and the dispersion of GLDM properties [J, K_0, $\Delta K_{\rm sym}(L)$] associated with the different models (see text). Nuclear models: Skyrme (filled symbols), relativistic (open symbols), and BHF-2 (star).

To summarize, if we characterize the L-P_{tt} relation using a GLDM development around saturation density, we can identify three effects that are crucial for the determination of $\delta P/\delta L$: (i) the explicit L dependence of the pressure given by Eq. (10); (ii) the L-ρ_{tt} correlation; and (iii) the L-$K_{\rm sym}$ correlation. These different contributions compensate each other. For some models (those of higher L), the GLDM predicts a decreasing $P_{tt}(L)$; for others (those of lower L), an increase would be obtained. It is interesting to note that $\delta P/\delta L$ cancels in the interval of the most realistic L values, namely, 50–80 MeV. By estimating an uncertainty of about 20% on the slopes of the L-ρ_{tt} and L-$K_{\rm sym}$ linear fits, we obtain an error bar of ± 0.02 fm^{-3} on $\delta P/\delta L$, which appears compatible with zero throughout this interval. These results are not a quantitative prediction on the evolution of the transition pressure with L; however, they show that the link between L and P_{tt} can not be deduced from qualitative arguments and, therefore, it is not soundly based. The relation between L and P_{tt} is, in fact, very sensitive to model dependence, as will be further discussed in the following.

C. Predictions of a standard GLDM

In order to study how the different GLDM coefficients can affect the core-crust transition, we will make use of a schematic model corresponding to a $D_3(\rho_0)$ expansion with typical values for the different coefficients. The choice of these values is illustrated in Fig. 11, which gives a graphical representation of the saturation properties of the different nuclear models considered in this paper. The lines indicate the intervals of coefficients attributed to the typical GLDM that we are now constructing. We define a reference $D_3(\rho_0)$ model characterized by the following parameters:

$$\rho_0 = 0.16\ \text{fm}^{-3},\ \ K_0 = 240\ \text{MeV},$$
$$Q_0 = -350\ \text{MeV},\ \ J = 31\ \text{MeV}\ .$$

The coefficient L varies in the interval [40; 100] MeV, and determines $K_{\rm sym}$ and $Q_{\rm sym}$ according to the relations

$$K_{\rm sym}(L) = a_{\rm K} \times L + b_{\rm K}, \quad (a_{\rm K}; b_{\rm K}) = (3.33; -281),$$
$$Q_s(L) = a_{\rm Q} \times L + b_{\rm Q}, \quad (a_{\rm Q}; b_{\rm Q}) = (-6.63; 765).$$

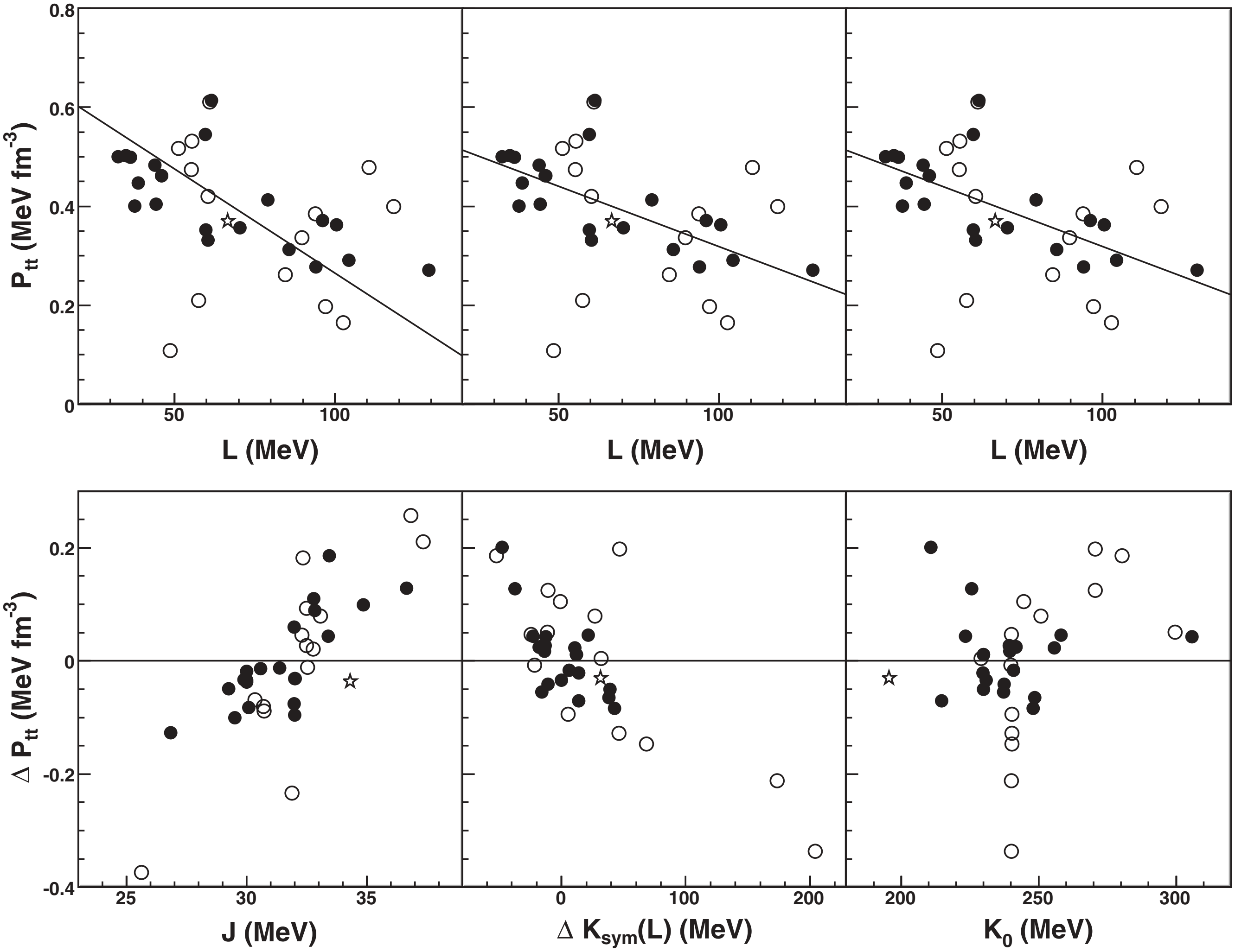

FIG. 15. Relation between the dispersion of $P_{tt}(L)$ and the dispersion of GLDM properties [J, K_0, $\Delta K_{\mathrm{sym}}(L)$] associated with the different models (see text). Nuclear models: Skyrme (filled symbols), relativistic (open symbols), and BHF-2 (star).

The predictions of this standard model for $\rho_{tt}(L)$, $Y_{p,tt}(L)$, and $P_{tt}(L)$ are represented in Fig. 12. As expected, we obtain a clear decrease of ρ_{tt} and $Y_{p,tt}$ with L, while the evolution of P_{tt} is quite flat. In the following, we will observe how these curves evolve when some of the standard EOS properties are modified within a realistic interval. We will modify separately the symmetry energy J, the incompressibility K_0, and the L-K_{sym} relation. On the left panel of Fig. 12, we show the effect of varying J between 29 and 33 MeV. On the right panel, we show the effect of varying K_0 between 220 and 260 MeV. On the central panel, we modify the linear relation between L and K_{sym} by adopting different values of $(a_{\mathrm{K}}; b_{\mathrm{K}})$: a softer version $(a_{\mathrm{K}}; b_{\mathrm{K}})_{\mathrm{soft}} = (2.8; -235)$ and a stiffer one $(a_{\mathrm{K}}; b_{\mathrm{K}})_{\mathrm{stiff}} = (3.8; -320)$.

The main features to be noted concerning the results of the standard schematic model and how they are affected by typical variations of the GLDM coefficients are as follows: (i) The qualitative behavior of ρ_{tt} and $Y_{p,tt}$ is maintained; although the absolute value can be affected by different aspects of the functional, they always unambiguously decrease with increasing L. (ii) The qualitative behavior of P_{tt} is very sensitive to the values of the GLDM coefficients; the application of a very moderate variation, inside a realistic model uncertainty, leads to opposite predictions: $P_{tt}(L)$ either increases or decreases, and most often it is quite flat. These two conclusions confirm the previous analysis.

IV. PARAMETRIZATION OF THE CORE-CRUST TRANSITION

In this section, we explore the possibility to reduce the model dispersion in the prediction of the core-crust transition by taking into account the effect of coefficients other than L. First, we check to what extent the dispersion in the L dependence of ρ_{tt}, $Y_{p,tt}$, and P_{tt} can be attributed to specific GLDM coefficients, such as the symmetry energy at saturation J, the incompressibility K_0, or the quantity $\Delta K_{\mathrm{sym}}(L) = K_{\mathrm{sym}} - (a_{\mathrm{K}} \times L + b_{\mathrm{K}})$. This last quantity characterizes the eccentricity of the model with respect to the typical relation

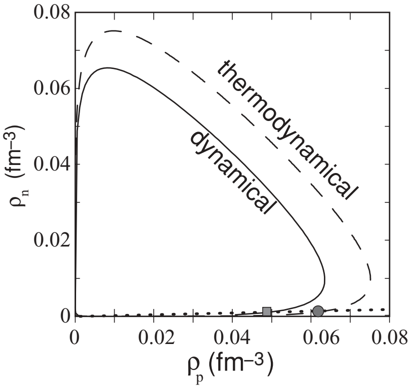

FIG. 16. Comparison between the thermodynamic (dashed line) and dynamic (solid line) spinodals. The dotted line represents the β-equilibrium EOS and the square and dot define the crust-core transition within, respectively, the dynamical and thermodynamical spinodals.

$K_{\text{sym}}(L) = (a_K \times L + b_K)$. On the basis of these results, we propose to fit the core-crust transition properties by a linear dependence on pairs of GLDM coefficients. This idea is applied to the thermodynamical transition, which has been the framework of our analysis, and to the dynamic transition, which is the best approximation to the realistic core-crust transition.

A. Role of the first GLDM coefficients in the dispersion

As we have seen in the previous section, the correlations between L and the core-crust transition properties ρ_{tt}, $Y_{p,tt}$, and P_{tt} suffer from a certain amount of dispersion when different kinds of models are considered. This effect is particularly harmful for the prediction of the transition pressure; with the link between L and P_{tt} being very sensitive to the details of the functional, the model dispersion destroys the possibility to deduce the value of P_{tt} from a measurement of L. In order to look for model properties that may be responsible for this dispersion, we first use the following procedure:

(i) We call M the GLDM model property, the effects of which are investigated, namely, J, K_0, or ΔK_{sym}.
(ii) We represent the quantities $X(L)$ calculated with the different models, with $X = Y_{p,tt}$ (Fig. 13), ρ_{tt} (Fig. 14), and P_{tt} (Fig. 15).

For each M property (J, K_0, or ΔK_{sym}), we check whether the diagram $X(L)$ can be separated in two regions associated with larger and smaller values of M:

(i) We use a trial frontier, namely, a straight line Λ: $X_\Lambda = a \times L + b$.
(ii) We calculate the distance of each data point i to this frontier: $[\Delta X]_{\Lambda,i} = X_i - (a \times L_i + b)$.
(iii) We vary the frontier Λ in order to obtain the best correlation for the diagram $[\Delta X]_\Lambda(M)$.

In this way, a different line Λ is defined for each model property M under study. This is clearly seen in Figs. 13, 14, and 15, where the frontier line in the three top graphs, associated, respectively, with $M = J,\ \Delta K_{\text{sym}},\ K_0$, differs from one graph to the other.

If the dispersion of the data points can be mainly attributed to differences in their respective M values, the diagram $[\Delta X]_\Lambda(M)$ must present a clear correlation. In this case, it would be sufficient to know the values of L and M of a given model to predict accurately the corresponding X value. On the contrary, if the diagram $[\Delta X]_\Lambda(M)$ appears completely uncorrelated, we can deduce that the coefficient M under study is not responsible for the dispersion of the data $X_i(L_i)$. In several cases, we find an intermediate situation in which the correlation of $[\Delta X]_\Lambda(M)$ is weak but allows us to associate eccentric values of M with large values of ΔX.

The most favorable situation appears in Fig. 13 with the effect of J on $\Delta Y_{p,tt}$. This effect was expected : $Y_{p,tt}$ depends on the value of the symmetry energy at subsaturation, which is well correlated with L as long as the different models have a similar symmetry energy at ρ_0. J also appears to affect

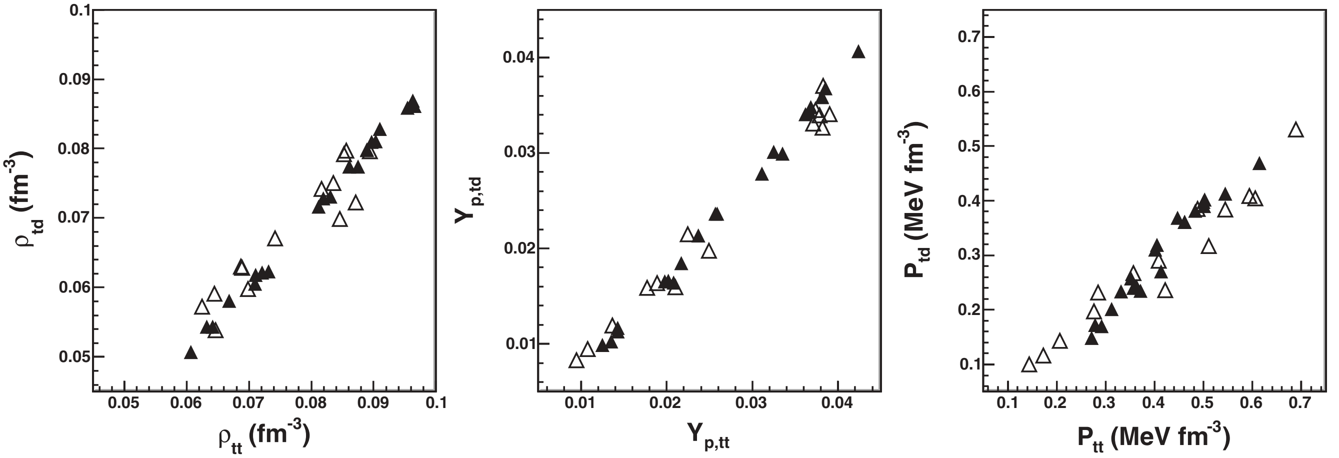

FIG. 17. Comparison between the transition taken at dynamic (td) and thermodynamic (tt) spinodal for different Skyrme (filled symbols) and relativistic (open symbols) models: density (left), proton fraction (center), and pressure (right).

TABLE III. Root mean square of residuals associated with two-variable linear fits $X_{ti} = a_1 \times M_1 + a_2 \times M_2 + b$, where $X_{ti} = \{\rho_{tt}, Y_{p,tt}, P_{tt}; \rho_{td}, Y_{p,td}, P_{td}\}$ and M_i are two of the isovector GLDM coefficients: $J_{\rm ref} = S(\rho_{\rm ref})$, $L_{\rm ref} = 3\rho_{\rm ref}[\partial S/\partial\rho](\rho_{\rm ref})$, and $K_{\rm sym,ref} = (3\rho_{\rm ref})^2[\partial^2 S/\partial\rho^2](\rho_{\rm ref})$. J, L, and $K_{\rm sym}$ are taken at $\rho_{\rm ref} = \rho_0$; J_{01}, L_{01}, and $K_{\rm sym,01}$ are taken at $\rho_{\rm ref} = 0.1$ fm^{-3}. The results for single-variable linear fits in function of L and L_{01} are also shown.

X$_{tt}$	M_1	M_2	rms	X_{td}	M_1	M_2	rms
ρ_{tt}	L		0.0038 fm^{-3}	ρ_{td}	L		0.0037 fm^{-3}
ρ_{tt}	J	L	0.0028 fm^{-3}	ρ_{td}	J	L	0.0035 fm^{-3}
ρ_{tt}	L	$K_{\rm sym}$	0.0038 fm^{-3}	ρ_{td}	L	$K_{\rm sym}$	0.0037 fm^{-3}
ρ_{tt}	L_{01}		0.0062 fm^{-3}	ρ_{td}	L_{01}		0.0054 fm^{-3}
ρ_{tt}	J_{01}	L_{01}	0.0037 fm^{-3}	ρ_{td}	J_{01}	L_{01}	0.0038 fm^{-3}
ρ_{tt}	L_{01}	$K_{\rm sym,01}$	0.0032 fm^{-3}	ρ_{td}	L_{01}	$K_{\rm sym,01}$	0.0037 fm^{-3}
$Y_{p,tt}$	L		0.0063	$Y_{p,td}$	L		0.0057
$Y_{p,tt}$	J	L	0.0022	$Y_{p,td}$	J	L	0.0024
$Y_{p,tt}$	L	$K_{\rm sym}$	0.0063	$Y_{p,td}$	L	$K_{\rm sym}$	0.0058
$Y_{p,tt}$	L_{01}		0.0081	$Y_{p,td}$	L_{01}		0.0074
$Y_{p,tt}$	J_{01}	L_{01}	0.0016	$Y_{p,td}$	J_{01}	L_{01}	0.0014
$Y_{p,tt}$	L_{01}	$K_{\rm sym,01}$	0.0040	$Y_{p,td}$	L_{01}	$K_{\rm sym,01}$	0.0040
P_{tt}	L		0.117 MeV fm^{-3}	P_{td}	L		0.085 MeV fm^{-3}
P_{tt}	J	L	0.076 MeV fm^{-3}	P_{td}	J	L	0.055 MeV fm^{-3}
P_{tt}	L	$K_{\rm sym}$	0.092 MeV fm^{-3}	P_{td}	L	$K_{\rm sym}$	0.067 MeV fm^{-3}
P_{tt}	L_{01}		0.129 MeV fm^{-3}	P_{td}	L_{01}		0.101 MeV fm^{-3}
P_{tt}	J_{01}	L_{01}	0.088 MeV fm^{-3}	P_{td}	J_{01}	L_{01}	0.069 MeV fm^{-3}
P_{tt}	L_{01}	$K_{\rm sym,01}$	0.036 MeV fm^{-3}	P_{td}	L_{01}	$K_{\rm sym,01}$	0.033 MeV fm^{-3}

the values of ρ_{tt} (Fig. 14) and P_{tt} (Fig. 15), although the correlation $[\Delta X]_\Lambda(J)$ is weaker in these two cases. Let us now consider the eccentricity of the $K_{\rm sym}$ behavior, namely, $\Delta K_{\rm sym}$. It has a clear effect on the relation $P_{tt}(L)$, as we see in Fig. 15; this confirms the analysis of the previous section, where we have underlined the role of the L-$K_{\rm sym}$ correlation in the link between L and P_{tt}. On the other hand, $\Delta K_{\rm sym}$ is uncorrelated with the position of the transition ρ_{tt} and $Y_{p,tt}$. Finally, the isoscalar incompressibility K_0 has no clear effect on the core-crust transition. It appears completely uncorrelated with the values of $Y_{p,tt}$ and P_{tt}. A weak correlation appears with ρ_{tt}, but this does not affect significantly the quality of the L-ρ_{tt} correlation. In the following, we will concentrate exclusively on the role of isovector coefficients.

B. Prediction of the dynamical core-crust transition

Until now, we have studied the quantities $X_{tt} = \{\rho_{tt}, Y_{p,tt}, P_{tt}\}$, which are defined by the crossing between the β-equilibrium condition and the thermodynamic spinodal. This framework allowed us to emphasize the analytical role of bulk GLDM coefficients in the transition. However, realistic descriptions of the core-crust transition involve stability comparison between homogeneous matter and clusterized matter. Equilibrium calculations have been performed, e.g., in Refs. [2,15–17]; it has been verified that the resulting transition can be very well approximated by the crossing between the β-equilibrium condition and the dynamic spinodal. In Fig. 16, we illustrate the differences between the thermodynamic and dynamic spinodals and identify with a square (dynamic) and dot (thermodynamic) the crust-core transition, defined by the crossing of the β-equilibrium EOS and the spinodal. We denote $X_{td} = \{\rho_{td}, Y_{p,td}, P_{td}\}$ as the quantities taken at this dynamic spinodal border. We have obtained these quantities within the effective Skyrme and relativistic approaches. The dynamic spinodal has not been calculated in the BHF framework since the BHF-based density functional does not include the density-gradient terms needed to modelize the surface effects associated with finite-size density fluctuations.

To check that the thermodynamic framework effectively reflects the correlations between the GLDM coefficients and the core-crust transition, we have to make sure that the transformation from X_{tt} to X_{td} does not destroy these correlations. This is verified in Fig. 17, where we plot the dynamic results as a function of the thermodynamic ones: we observe that these quantities are strongly correlated. In the following, we will extract some empirical relations between the GLDM coefficients and the dynamic core-crust properties $\{\rho_{td}, Y_{p,td}, P_{td}\}$.

A systematic analysis of the effect of the isovector coefficients J, L, and $K_{\rm sym}$ on the transition properties is presented in Table III. Our previous study has shown that the relation $X_{tt}(L)$ is affected by atypical values of J and $K_{\rm sym}$ associated with the various models. To explore this effect, we have performed two-dimensional fits of the transition data

$$X_{ti}(M_1, M_2) = a_1 M_1 + a_2 M_2 + b\,, \qquad (16)$$

where $X_{ti} = \{\rho_{tt}, Y_{p,tt}, P_{tt}; \rho_{td}, Y_{p,td}, P_{td}\}$ (dynamic or thermodynamic transition), and M_i are two of the isovector GLDM coefficients: $J_{\rm ref} = S(\rho_{\rm ref})$, $L_{\rm ref} = 3\rho_{\rm ref}[\partial S/\partial\rho](\rho_{\rm ref})$, and $K_{\rm sym,ref} = (3\rho_{\rm ref})^2[\partial^2 S/\partial\rho^2](\rho_{\rm ref})$. We have considered the saturation coefficients J, L, and $K_{\rm sym}$, as well as coefficients at the reference density $\rho_{\rm ref} = 0.1$ fm^{-3}, denoted J_{01}, L_{01}, and $K_{\rm sym,01}$. Table III gives the root mean square (rms) of residuals associated with the different fits, indicating the

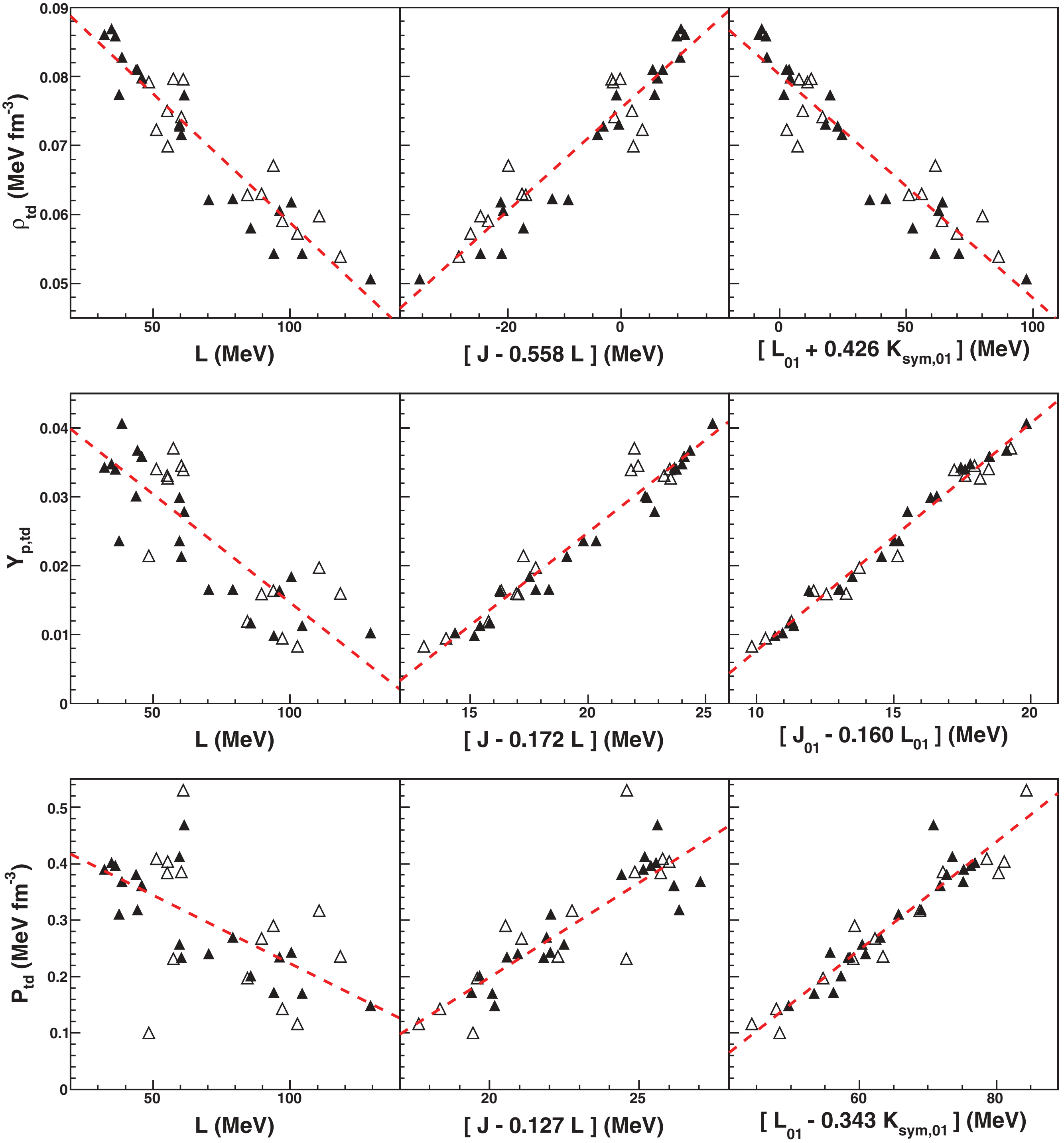

FIG. 18. (Color online) Correlations between the dynamic core-crust transition properties and GLDM coefficients (see text).

relevance of the respective combinations of coefficients in the determination of X_{ti}.

It appears that ρ_{ti} is well correlated with L; no significant improvement can be obtained by considering pairs of coefficients. The quality of the L-ρ_{ti} correlation can be understood as a consequence of Eq. (9), as discussed in Sec. III A. In the cases of $Y_{p,ti}$ and P_{ti}, however, the predictions can be considerably improved by using combinations of coefficients. As expected, $Y_{p,ti}$ is very well correlated with a combination of J and L, and this result is still improved using a combination of J_{01} and L_{01}. On the other hand, the values of Table III indicate that combinations of L and $K_{\rm sym}$ are not relevant to determine $Y_{p,ti}$. The transition pressure, instead, presents improved correlations with two kinds of parameter combinations: either J and L at saturation density or L_{01} and $K_{{\rm sym},01}$, and the latter leads to the smallest rms of residuals.

We show in Fig. 18 the most significant correlations obtained between the dynamic transition properties and different combinations of the GLDM coefficients. The quantities ρ_{td}, $Y_{p,td}$, and P_{td} are shown as a function of L and as a function of selected coefficient combinations. For the transition density, we verify the good L-ρ_{td} correlation; we also consider two coefficient combinations $[J - 0.558 \times L]$ and $[L_{01} + 0.426 \times K_{\mathrm{sym},01}]$, which lead to a similar dispersion, lower than ± 0.004 fm^{-3}. The situation is different for the proton fraction $Y_{p,td}$ and the pressure P_{td} for which the correlation with L is not so good. The selected coefficient combinations lead to clearly improved correlations. Concerning the proton fraction, the combinations $[J - 0.172 \times L]$ and especially $[J_{01} - 0.160 \times L_{01}]$ present excellent correlations with $Y_{p,td}$. As for the transition pressure, the combinations $[J - 0.127 \times L]$ and $[L_{01} - 0.343 \times K_{\mathrm{sym},01}]$ allow us to considerably reduce the data dispersion and show unambiguous correlations with P_{td}; this is especially true for the second combination (coefficients extracted at 0.1 fm^{-3}), for which the typical model dispersion for P_{td} becomes ± 0.033 MeV fm^3 instead of ± 0.085 MeV fm^3 in the case of $P_{td}(L)$. The linear fits represented in Fig. 18 are

$$\rho_{td}(L) = (-3.75 \times 10^{-4} \times L + 0.0963)\ \mathrm{fm}^{-3}, \tag{17}$$

$$\rho_{td}(J, L) = (7.46 \times 10^{-4} \times [J - 0.558 \times L] + 0.0754)\ \mathrm{fm}^{-3}, \tag{18}$$

$$\rho_{td}(L_{01}, K_{\mathrm{sym},01}) = (3.23 \times 10^{-4} \times [L_{01} + 0.426 \times K_{\mathrm{sym},01}] + 0.0802)\ \mathrm{fm}^{-3}, \tag{19}$$

$$Y_{p,td}(L) = -3.15 \times 10^{-4} \times L + 0.0461, \tag{20}$$

$$Y_{p,td}(J, L) = 2.69 \times 10^{-3} \times [J - 0.172 \times L] - 0.0290, \tag{21}$$

$$Y_{p,td}(J_{01}, L_{01}) = 3.30 \times 10^{-3} \times [J_{01} - 0.160 \times L_{01}] - 0.0253, \tag{22}$$

$$P_{td}(L) = (-2.42 \times 10^{-3} \times L + 0.465)\ \mathrm{MeV\ fm}^{-3}, \tag{23}$$

$$P_{td}(J, L) = (3.36 \times 10^{-2} \times [J - 0.127 \times L] - 0.474)\ \mathrm{MeV\ fm}^{-3}, \tag{24}$$

$$P_{td}(L_{01}, K_{\mathrm{sym},01}) = (9.59 \times 10^{-3} \times [L_{01} - 0.343 \times K_{\mathrm{sym},01}] - 0.328)\ \mathrm{MeV\ fm}^{-3}. \tag{25}$$

The relations involving GLDM coefficients at $\rho = 0.1$ fm^{-3} allow us to predict the core-crust transition density, asymmetry, and pressure within a reasonable model uncertainty. This indicates that exploring the subsaturation properties of nuclei in order to constrain directly these low-density coefficients could allow us to modelize core-crust transition properties that do not depend strongly on the type of nuclear functional that is used.

V. CONCLUSION

In this paper, we have studied to what extent the core-crust transition properties can be predicted by using a reduced set of phenomenological constraints. Different kinds of nuclear models have been compared: Skyrme and relativistic effective models and a microscopic BHF approach. It is seen that the EOS obtained in the relativistic cases present much more variability in their density dependence than the Skyrme cases due to different ways of describing the interaction; notably, a softer symmetry energy is obtained with density-dependent couplings, and the inclusion of the delta meson leads to an atypical density evolution of the symmetry-energy slope, as was noticed in Ref. [26]. A more regular behavior is observed within the Skyrme sets of parameters; this has the drawback to bring possibly spurious correlations between the EOS properties at saturation and subsaturation density. As for the BHF calculations, although microscopic approaches are indispensable to provide realistic predictions for the EOS away from the phenomenological constraints, their predictions for the core-crust transition properties are very sensitive to the numerical fit of the EOS, which is necessary to determine its curvature. However, other ways could be followed to constrain the curvature properties from microscopic approaches, such as the study of Landau parameters [29,30].

To relate the predictions of the different models with their properties at a fixed density, we have introduced a generalized liquid-drop model (GLDM), which consists of a density development of the EOS around a reference density ρ_{ref}, up to a chosen order. When ρ_{ref} is the saturation density, we have seen that a development up to order 3 is necessary to get reasonably close to the thermodynamic core-crust transition properties predicted by the complete functionals. This means that the correlations that can be observed between the symmetry-energy slope at saturation L and the core-crust transition properties are subjected to further correlations existing between the various coefficients of the GLDM. Such correlations reflect two kinds of effects: (i) the possible existence of effective constraints at subsaturation densities, arising from the nuclear data used in the fit of most of the effective models, and (ii) the regularity of the functional shapes, which depend on the construction of the model. We have also considered a development at a lower reference density $\rho_{\mathrm{ref}} = 0.1$ fm^{-3}. This approach has the advantage of reducing the model dependence arising from specific functional shapes and of focusing on a density region closer to most nucleus observations. A development at order 2 around $\rho = 0.1$ fm^{-3} allows us to characterize the thermodynamic core-crust transition within nearly the smallest uncertainty allowed by a GLDM approach. This smallest uncertainty is given by the infinite development D_∞, which gives the best GLDM approximation of the complete functional by neglecting only the extra-parabolic terms in the isospin dependence of the nuclear interaction.

We have also presented a more detailed study of the relation between L and the core-crust transition, the conclusions of which confirm our previous analysis [12]. Namely, the core-crust transition density ρ_{tt} and proton fraction $Y_{p,tt}$ appear clearly correlated with L, despite the variety of models, while the link between L and the transition pressure P_{tt} is much more sensitive to model dependence. Indeed, the impact of L on the transition pressure involves several opposite contributions, which tend to compensate each other; thus, it is not possible to establish a qualitative prediction for the evolution $P_{tt}(L)$, which can change sign depending on the model (see, for instance, the opposite predictions presented in Refs. [10,11]).

To explore the possibility to overcome the model dispersion and predict the core-crust transition properties from a reduced set of nuclear constraints, we have searched those GLDM coefficients other than L that play a major role in the determination of this transition: J and K_{sym} were found to have a significant responsibility in the observed dispersion. Finally, we have addressed the case of the dynamic core-crust transition given by the crossing between the dynamic spinodal and the β equilibrium. This corresponds to a realistic approximation of the actual core-crust transition, and takes place at lower density than in the thermodynamic approach. We have verified that the dynamic transition is related to the GLDM coefficients by similar correlations. The L-ρ_{td} correlation is quite good, and it can not be significantly improved by considering other coefficients; however, the predictivity of $Y_{p,td}$ and P_{td} is considerably better in terms of selected pairs of coefficients. An excellent correlation appears between $Y_{p,td}$ and a combination of J and L, and it is even better using a combination of J_{01} and L_{01} (coefficients defined at $\rho_{\text{ref}} = 0.1$ fm^{-3}). Furthermore, the model dependence in the prediction of the transition pressure can be considerably reduced if we consider a combination of L_{01} and $K_{\text{sym},01}$. In this case, an unambiguous correlation is obtained within all the varieties of Skyrme and relativistic models considered.

To conclude, it appears that an accurate determination of the first three GLDM coefficients at $\rho_{\text{ref}} = 0.1$ fm^{-3} would allow a prediction of the core-crust transition properties that do not depend much on the model construction. This gives a strong motivation to focus on the relation between nuclear observables and GLDM coefficients at subsaturation density. It will become possible to use phenomenological nuclear models to restrict the range of the core-crust transition properties in neutron stars; this would have an impact on the interpretation of astrophysical observations, and on the possible scenarios to explain phenomena such as pulsar glitches [13,14]. As discussed in [13], the transition pressure is an essential input to infer the neutron-star mass-radius relation from glitch observations. Since the mass-radius relation predicted by a given EOS is mainly determined by its high-density region, an accurate prediction of the transition pressure would also constrain the high-density EOS.

ACKNOWLEDGMENTS

This work was partially supported by the ANR NExEN contract, FCT (Portugal) under Grants No. SFRH/BPD/46802/2008, No. FCOMP-01-0124-FEDER-008393 with FCT reference No. CERN/FP/109316/2009, No. PTDC/FIS/64707/2006, No. PTDC/FIS/113292/2009, and COMPSTAR, an ESF Research Networking Programme.

APPENDIX: NUCLEAR MODELS

In this appendix, we give an overview of the different types of nuclear models, the properties of which are compared in this paper. Each of these models gives at every density the energy of symmetric matter and the symmetry energy (in contrast with the GLDM exposed in the Sec. II A, which is based on a density expansion).

A. Skyrme-type effective models

The local Skyrme interaction [31] allows us to define an energy density functional $\mathcal{H}(\mathbf{r})$ such that the total energy for a system of nucleons in a Slater determinant $|\psi\rangle$ reads as

$$\langle\psi|\hat{H}|\psi\rangle = \int \mathcal{H}(\mathbf{r}) d^3r \, . \tag{A1}$$

For homogeneous, spin-saturated matter with no Coulomb interaction, the Skyrme energy density functional is composed of four terms:

$$\mathcal{H} = \mathcal{K} + \mathcal{H}_0 + \mathcal{H}_3 + \mathcal{H}_{\text{eff}}. \tag{A2}$$

In this expression, $\mathcal{K}$ is the kinetic-energy term, $\mathcal{H}_0$ is a density-independent two-body term, $\mathcal{H}_3$ is a density-dependent term, and $\mathcal{H}_{\text{eff}}$ is a momentum-dependent term [32]:

$$\mathcal{K} = \frac{\tau}{2m}, \tag{A3}$$

$$\mathcal{H}_0 = C_0\rho^2 + D_0\rho_3^2, \tag{A4}$$

$$\mathcal{H}_3 = C_3\rho^{\sigma+2} + D_3\rho^{\sigma}\rho_3^2, \tag{A5}$$

$$\mathcal{H}_{\text{eff}} = C_{\text{eff}}\rho\tau + D_{\text{eff}}\rho_3\tau_3 \, . \tag{A6}$$

We have introduced the isoscalar and isovector particle densities ρ and ρ_3 as well as kinetic densities τ and τ_3:

$$\begin{aligned} \rho &= \rho_n + \rho_p, \quad \tau = \tau_n + \tau_p, \\ \rho_3 &= \rho_n - \rho_p, \quad \tau_3 = \tau_n - \tau_p, \end{aligned} \tag{A7}$$

where, denoting q the third component of the isospin (n for neutrons and p for protons), the kinetic densities are defined by $\tau_q = \langle\hat{k}^2\rangle_q$. The coefficients C and D, associated, respectively, with the isoscalar and isovector contributions, are linear combinations of the traditional Skyrme parameters

$$\begin{aligned} C_0 &= 3t_0/8, \\ D_0 &= -t_0(2x_0+1)/8, \\ C_3 &= t_3/16, \\ D_3 &= -t_3(2x_3+1)/48, \\ C_{\text{eff}} &= [3t_1 + t_2(4x_2+5)]/16, \\ D_{\text{eff}} &= [t_2(2x_2+1) - t_1(2x_1+1)]/16. \end{aligned} \tag{A8}$$

In this paper, we have considered 21 Skyrme parametrizations, commonly used in the literature, chosen in order to cover a wide range of L values while presenting acceptable saturation properties. Traditionally, Skyrme parameters are fitted in order to reproduce selected nuclear properties measured in a set of nuclei: basically masses and radii, plus several other input with increasing level of sophistication. SV [33] is among the earlier parametrizations. SGII [34], for which spin properties have also been used as constraints, can reproduce isospin effects in giant dipole resonances. R_σ and G_σ [35] consider spin-orbit splitting in ^{16}O and surface widths. SkMP [36] was built to improve the fit of ^{208}Pb charge distribution. The series SkI2, SkI3, SkI4, SkI5 [37], and SkI6 [38] include constraints on the isotope shifts of the charge radius in Pb and Ca. SkO [39] further considers isotopic evolution of two-neutron separation energies in Pb. In addition to nuclear data constraints, many Skyrme forces include in their fitting procedure the neutron-matter EOS from microscopic calculations; the objective is to obtain a reliable behavior of the density functional at high isospin asymmetry, especially for astrophysical applications. RATP [40] was the first parametrization using this procedure, including the neutron-matter calculation by Friedman and Pandharipande [41]. The Skyrme-Lyon forces SLy230a, SLy230b [32], SLy4 [42], and SLy10 [43] use the pure neutron-matter equation of state UV14 + UVII by R.B. Wiringa *et al.* [44]. NRAPR [45] (nonrelativistic APR) stands for the Skyrme interaction parameters obtained from a fit of the APR equation of state (Akmal-Pandharipande-Ravenhall, Ref. [46]). LNS [47] is based on Brueckner-Hartree-Fock calculations of infinite nuclear matter at different values of isospin asymmetry. The Bruxelles-Skyrme forces BSk14 [48], BSk16 [49], and BSk17 [50] include the Friedman and Pandharipande calculation of neutron matter [41], and a HFB treatment of pairing effects in order to improve mass predictions in the neutron-drip region.

B. Relativistic effective models

In this paper, we consider two kinds of relativistic effective approaches: RMF models, which have constant coupling parameters described by the Lagrangian density of nonlinear Walecka models (NLWM), and DDH models with density-dependent coupling parameters. In each case, we consider models including or not the δ meson, which have been introduced to include in the isovector channel the same symmetry existing already in the isoscalar channel with the meson pair (σ, ω) responsible for saturation in RMF models [51]. The presence of the δ meson softens the symmetry energy at subsaturation densities and hardens it above saturation density. The RMF parametrizations we use are NL3 [52], TM1 [53], GM1, GM3 [54], FSU [55], NL$\omega\rho$ [56], and NL$\rho\delta$ [57]. The DDH parametrizations are TW [58], DD-ME1, DD-ME2 [59], and DDHδ [60]. The models NL$\rho\delta$(0) and NL$\rho\delta$(2.5) introduced in [57] have the same isoscalar properties and the same symmetry energy at saturation, however, the last model includes the δ meson with $g_\delta = 2.5$, while in the first one, the δ coupling was set to zero. We have also introduced the parametrization NL$\rho\delta$(1.7) with a weaker δ-meson coupling (1.7 instead of 2.5). The model NL$\omega\rho$(025) includes a $\omega\rho$ nonlinear term in the Lagrangian as in [56] with strength $\Lambda_v = 0.025$. The parametrization DDHδI-25 introduced in [60] has a quite low symmetry energy at saturation (25 MeV); therefore, we also consider the parametrization DDHδII-30 where the ρ-meson coupling was adjusted so that, at saturation, the symmetry energy is 30 MeV, and all the isoscalar properties are kept fixed.

The relativistic approach is based on a Lagrangian density given by

$$\mathcal{L} = \sum_{i=p,n} \mathcal{L}_i + \mathcal{L}_\sigma + \mathcal{L}_\omega + \mathcal{L}_\rho + \mathcal{L}_{\omega\rho} + \mathcal{L}_\delta \, . \tag{A9}$$

The nucleon Lagrangians read as

$$\mathcal{L}_i = \bar{\psi}_i [\gamma_\mu i D^\mu - \mathcal{M}^*] \psi_i \, , \tag{A10}$$

with

$$i D^\mu = i\partial^\mu - \Gamma_v V^\mu - \frac{\Gamma_\rho}{2} \vec{\tau} \cdot \vec{b}^\mu , \tag{A11}$$

$$\mathcal{M}^* = m - \Gamma_s \phi - \Gamma_\delta \vec{\tau} \cdot \vec{\delta} \, , \tag{A12}$$

where $\vec{\tau}$ is the isospin operator. We use the vector symbol to designate a vector in isospin space.

The isoscalar part is associated with the scalar sigma (σ) field ϕ and the vector omega (ω) field V_μ, while the isospin dependence comes from the isovector-scalar delta (δ) field δ^i and the isovector-vector rho (ρ) field b^i_μ (where μ is a space-time index and i an isospin-direction index). The associated Lagrangians are

$$\begin{aligned}
\mathcal{L}_\sigma &= +\tfrac{1}{2}\left(\partial_\mu \phi \partial^\mu \phi - m_s^2 \phi^2\right) - \tfrac{1}{3!}\kappa \phi^3 - \tfrac{1}{4!}\lambda \phi^4 , \\
\mathcal{L}_\omega &= -\tfrac{1}{4}\Omega_{\mu\nu}\Omega^{\mu\nu} + \tfrac{1}{2} m_v^2 V_\mu V^\mu + \tfrac{1}{4!}\xi g_v^4 (V_\mu V^\mu)^2 , \\
\mathcal{L}_\delta &= +\tfrac{1}{2}(\partial_\mu \vec{\delta} \partial^\mu \vec{\delta} - m_\delta^2 \vec{\delta}^2), \\
\mathcal{L}_\rho &= -\tfrac{1}{4}\vec{B}_{\mu\nu} \cdot \vec{B}^{\mu\nu} + \tfrac{1}{2} m_\rho^2 \vec{b}_\mu \cdot \vec{b}^\mu , \\
\mathcal{L}_{\omega\rho} &= g_\rho^2 \mathbf{b}_\mu \cdot \mathbf{b}^\mu \Lambda_v g_v^2 V_\mu V^\mu ,
\end{aligned}$$

where $\Omega_{\mu\nu} = \partial_\mu V_\nu - \partial_\nu V_\mu$, $\vec{B}_{\mu\nu} = \partial_\mu \vec{b}_\nu - \partial_\nu \vec{b}_\mu - \Gamma_\rho(\vec{b}_\mu \times \vec{b}_\nu)$, and Γ_j and m_j are, respectively, the coupling parameters of the mesons $j = s, v, \delta, \rho$ with the nucleons and their masses. The self-interacting terms for the σ meson are included only for the NL3 and NLδ parametrizations, with κ and λ denoting the corresponding coupling constants.

The density-dependent coupling parameters Γ_s, Γ_v, and Γ_ρ are adjusted in order to reproduce some of the nuclear matter bulk properties, using the following parametrization:

$$\Gamma_i(\rho) = \Gamma_i(\rho_{sat}) f_i(x) \, , \quad i = s, v \tag{A13}$$

with

$$f_i(x) = a_i \frac{1 + b_i(x + d_i)^2}{1 + c_i(x + d_i)^2} \, , \tag{A14}$$

where $x = \rho/\rho_{sat}$ and

$$\Gamma_\rho(\rho) = \Gamma_\rho(\rho_{sat}) \exp[-a_\rho(x - 1)] \, . \tag{A15}$$

The values of the parameters m_i, Γ_i, a_i, b_i, c_i, and d_i, $i = s, v, \rho$, for TW and DD-ME2 are, respectively, given in [58] and [61] and for DDHδ in [60,62]. In this last case, the parametrization for the δ- and ρ-coupling parameters is also given by (A13) with

$$f_i(x) = a_i \exp[-b_i(x - 1)] - c_i(x - d_i) \, , \quad i = \rho, \, \delta .$$

The Γ_i coupling parameters are replaced by the g_i coupling constants in the NL3 and NLδ models.

C. The BHF approach of asymmetric nuclear matter

The BHF approach of asymmetric nuclear matter [63,64] starts with the construction of all the G matrices describing the effective interaction between two nucleons in the presence of a surrounding medium. They are obtained by solving the well-known Bethe-Goldstone equation

$$G_{\tau_1\tau_2;\tau_3\tau_4}(\omega) = V_{\tau_1\tau_2;\tau_3\tau_4} + \sum_{ij} V_{\tau_1\tau_2;\tau_i\tau_j} \frac{Q_{\tau_i\tau_j}}{\omega - \epsilon_i - \epsilon_j + i\eta} \times G_{\tau_i\tau_j;\tau 3\tau_4}(\omega), \quad \text{(A16)}$$

where $\tau = n, p$ indicates the isospin projection of the two nucleons in the initial, intermediate, and final states, V denotes the bare NN interaction, $Q_{\tau_i\tau_j}$ is the Pauli operator that allows only intermediate states compatible with the Pauli principle, and ω, the so-called starting energy, corresponds to the sum of nonrelativistic energies of the interacting nucleons. The single-particle energy ϵ_τ of a nucleon with momentum $\vec{k}$ is given by

$$\epsilon_\tau(\vec{k}) = \frac{\hbar^2 k^2}{2m_\tau} + \mathrm{Re}[U_\tau(\vec{k})] \ , \quad \text{(A17)}$$

where the single-particle potential $U_\tau(\vec{k})$ represents the mean field "felt" by a nucleon due to its interaction with the other nucleons of the medium. In the BHF approximation, $U(\vec{k})$ is calculated through the "on-shell energy" G matrix, and is given by

$$U_\tau(\vec{k}) = \sum_{\tau'} \sum_{|\vec{k}'|<k_{F_{\tau'}}} \langle \vec{k}\vec{k}' | G_{\tau\tau';\tau\tau'}[\omega = \epsilon_\tau(k) + \epsilon_{\tau'}(k')] | \vec{k}\vec{k}' \rangle_A, \quad \text{(A18)}$$

where the sum runs over all neutron- and proton-occupied states and where the matrix elements are properly antisymmetrized. We note here that the so-called continuous prescription has been adopted for the single-particle potential when solving the Bethe-Goldstone equation. As shown in Refs. [65,66], the contribution to the energy per particle from three-hole line diagrams is minimized in this prescription. Once a self-consistent solution of Eqs. (A16) and (A18) is achieved, the energy per particle can be calculated as

$$\frac{E}{A}(\rho, \beta) = \frac{1}{A} \sum_\tau \sum_{|\vec{k}|<k_{F_\tau}} \left(\frac{\hbar^2 k^2}{2m_\tau} + \frac{1}{2}\mathrm{Re}[U_\tau(\vec{k})] \right). \quad \text{(A19)}$$

The BHF calculation carried out in this paper uses the realistic Argonne V18 (Av18) [67] nucleon-nucleon interaction supplemented with a three-body force of Urbana type, which (for the use in BHF calculations) was reduced to a two-body density-dependent force by averaging over the third nucleon in the medium [68]. This three-body force contains two parameters that are fixed by requiring that the BHF calculation reproduces the energy and saturation density of symmetric nuclear matter. We note that more microscopically based three-body forces without adjustable parameters have been recently constructed (see Refs. [69–71] for a recent analysis of the use of three-body forces in nuclear and neutron matter). We note also that the Av18 interaction contains terms that break explicitly isospin symmetry. Therefore, in principle, we should consider also odd powers of y in the expansion (1) for the Brueckner calculation. However, we have neglected such terms since, as shown by Müther *et al.* in Ref. [72], the effects of isospin symmetry breaking on the symmetry energy are quite weak (less than 0.5 MeV for a wide range of NN interactions).

---

[1] A. W. Steiner *et al.*, Phys. Rep. **411**, 325 (2005).
[2] K. Oyamatsu and K. Iida, Phys. Rev. C **75**, 015801 (2007).
[3] B. A. Li, L. W. Chen, and C. M. Ko, Phys. Rep. **464**, 113 (2008).
[4] M. Centelles, X. Roca-Maza, X. Viñas, and M. Warda, Phys. Rev. Lett. **102**, 122502 (2009).
[5] A. Klimkiewicz *et al.*, Phys. Rev. C **76**, 051603 (2007).
[6] L. Trippa, G. Colo, and E. Vigezzi, Phys. Rev. C **77**, 061304 (2008).
[7] D. V. Shetty, S. J. Yennello, and G. A. Souliotis, Phys. Rev. C **75**, 034602 (2007); **76**, 024606 (2007).
[8] B. A. Li, G.-C. Yang, and W. Zuo, Phys. Rev. C **71**, 014608 (2005); M. B. Tsang *et al.*, Phys. Rev. Lett. **102**, 122701 (2009).
[9] C. J. Horowitz and J. Piekarewicz, Phys. Rev. Lett. **86**, 5647 (2001).
[10] J. Xu, L. W. Chen, B. A. Li, and H. R. Ma, Astrophys. J. **697**, 1549 (2009).
[11] Ch. C. Moustakidis, T. Nikšić, G. A. Lalazissis, D. Vretenar, and P. Ring, Phys. Rev. C **81**, 065803 (2010).
[12] C. Ducoin, J. Margueron, and C. Providência, Europhys. Lett. **91**, 32001 (2010).
[13] B. Link, R. I. Epstein, and J. M. Lattimer, Phys. Rev. Lett. **83**, 3362 (1999).
[14] J. Lattimer and M. Prakash, Phys. Rep. **333**, 121 (2000).
[15] T. Maruyama, T. Tatsumi, D. N. Voskresensky, T. Tanigawa, and S. Chiba, Phys. Rev. C **72**, 015802 (2005).
[16] S. S. Avancini, D. P. Menezes, M. D. Alloy, J. R. Marinelli, M. M. W. Moraes, and C. Providência, Phys. Rev. C **78**, 015802 (2008).
[17] S. S. Avancini, S. Chiacchiera, D. P. Menezes, and C. Providência, Phys. Rev. C **82**, 055807 (2010).
[18] C. J. Pethick, D. G. Ravenhall, and C. P. Lorentz, Nucl. Phys. A **584**, 675 (1995).
[19] L. Brito, C. Providência, A. M. Santos, S. S. Avancini, D. P. Menezes, and Ph. Chomaz, Phys. Rev. C **74**, 045801 (2006).
[20] C. Ducoin, Ph. Chomaz, and F. Gulminelli, Nucl. Phys. A **789**, 403 (2007).
[21] M. Baldo and C. Ducoin, Phys. Rev. C **79**, 035801 (2009).
[22] J. Piekarewicz and M. Centelles, Phys. Rev. C **79**, 054311 (2009).
[23] I. Vidaña, C. Providência, A. Polls, and A. Rios, Phys. Rev. C **80**, 045806 (2009).
[24] R. J. Furnstahl, Nucl. Phys. A **706**, 85 (2002).
[25] T. Nikšić, D. Vretenar, and P. Ring, Phys. Rev. C **78**, 034318 (2008).
[26] C. Ducoin, C. Providência, A. M. Santos, L. Brito, and Ph. Chomaz, Phys. Rev. C **78**, 055801 (2008).

[27] G. Colò, N. Van Giai, J. Meyer, K. Bennaceur, and P. Bonche, Phys. Rev. C **70**, 24307 (2004).
[28] I. Vidaña and A. Polls, Phys. Lett. B **666**, 232 (2008).
[29] M. Baldo and L. S. Ferreira, Phys. Rev. C **50**, 1887 (1994).
[30] U. Lombardo, Caiwan Shen, and W. Zuo, Phys. Rev. C **67**, 037301 (2003).
[31] D. Vautherin and D. M. Brink, Phys. Rev. C **3**, 626 (1972).
[32] E. Chabanat, P. Bonche, P. Haensel, J. Meyer, and R. Schaeffer, Nucl. Phys. A **627**, 710 (1997).
[33] M. Beiner, H. Flocard, Nguyen Van Giai, and P. Quentin, Nucl. Phys. A **238**, 29 (1975).
[34] Nguyen Van Giai and H. Sagawa, Phys. Lett. B **106**, 379 (1981).
[35] J. Friedrich and P.-G. Reinhard, Phys. Rev. C **33**, 335 (1986).
[36] L. Bennour, P. Bonche, J. Dobaczewski, and H. Flocard, Phys. Rev. C **40**, 2834 (1989).
[37] P.-G. Reinhard and H. Flocard, Nucl. Phys. A **584**, 467 (1995).
[38] W. Nazarewicz *et al.*, Phys. Rev. C **53**, 740 (1996).
[39] P.-G.Reinhard, D. J. Dean, W. Nazarewicz, J. Dobaczewski, J. A. Maruhn and M. R. Strayer, Phys. Rev. C **60**, 014316 (1999).
[40] M. Rayet, M. Arnould, G. Paulus, and F. Tondeur, Astron. Astrophys. **116**, 183 (1982).
[41] B. Friedman and V. R. Pandharipande, Nucl. Phys. A **361**, 502 (1981).
[42] E. Chabanat, P. Bonche, P. Haensel, J. Meyer, and R. Schaeffer, Nucl. Phys. A **635**, 231 (1997).
[43] E. Chabanat, Ph.D. thesis, Lyon University, 1995.
[44] R. B. Wiringa, V. Fiks, and A. Fabrocini, Phys. Rev. C **38**, 1010 (1988).
[45] A. W. Steiner, M. Prakash, J. M. Lattimer, and P. J. Ellis, Phys. Rep. **411**, 325 (2005).
[46] A. Akmal, V. R. Pandharipande, and D. G. Ravenhall, Phys. Rev. C **58**, 1804 (1998).
[47] L. G. Cao, U. Lombardo, C. W. Shen, and N. Van Giai, Phys. Rev. C **73**, 014313 (2006).
[48] S. Goriely, M. Samyn, and J. M. Pearson, Phys. Rev. C **75**, 064312 (2007).
[49] N. Chamel, S. Goriely, and J. M. Pearson, Nucl. Phys. A **812**, 72 (2008).
[50] S. Goriely, N. Chamel, and J. M. Pearson, Phys. Rev. Lett. **102**, 152503 (2009).
[51] B. Liu, V. Greco, V. Baran, M. Colonna, and M. Di Toro, Phys. Rev. C **65**, 045201 (2002).
[52] G. A. Lalazissis, J. König, and P. Ring, Phys. Rev. C **55**, 540 (1997).
[53] K. Sumiyoshi, H. Kuwabara, and H. Toki, Nucl. Phys. A **581**, 725 (1995).
[54] N. K. Glendenning and S. A. Moszkowski, Phys. Rev. Lett. **67**, 2414 (1991).
[55] B. G. Todd-Rutel and J. Piekarewicz, Phys. Rev. Lett. **95**, 122501 (2005).
[56] C. J. Horowitz and L. Piekarewicz, Phys. Rev. Lett. **86**, 5647 (2001).
[57] B. Liu, V. Greco, V. Baran, M. Colonna, and M. Di Toro, Phys. Rev. C **65**, 045201 (2002).
[58] S. Typel and H. H. Wolter, Nucl. Phys. A **656**, 331 (1999).
[59] T. Nikšić, D. Vretenar, P. Finelli, and P. Ring, Phys. Rev. C **66**, 024306 (2002); G. A. Lalazissis, T. Nikšić, D. Vretenar, and P. Ring, *ibid.* **71**, 024312 (2005).
[60] T. Gaitanos *et al.*, Nucl. Phys. A **732**, 24 (2004).
[61] T. Nikšić, D. Vretenar, and P. Ring, Phys. Rev. C **66**, 064302 (2002).
[62] S. S. Avancini, L. Brito, D. P. Menezes, and C. Providência, Phys. Rev. C **70**, 015203 (2004).
[63] I. Bombaci and U. Lombardo, Phys. Rev. C **44**, 1892 (1991).
[64] W. Zuo, I. Bombaci, and U. Lombardo, Phys. Rev. C **60**, 024605 (1999).
[65] H. Q. Song, M. Baldo, G. Giansiracusa, and U. Lombardo, Phys. Rev. Lett. **81**, 1584 (1998).
[66] M. Baldo, G. Giansiracusa, U. Lombardo, and H. Q. Song, Phys. Lett. B **473**, 1 (2000).
[67] R. B. Wiringa, V. G. J. Stoks, and R. Schiavilla, Phys. Rev. C **51**, 38 (1995).
[68] B. A. Loiseau, Y. Nogami, and C. K. Ross, Nucl. Phys. A **165**, 601 (1971); **176**, 665(E) (1971); P. Grangé, M. Martzolff, Y. Nogami, D. W. L. Sprung, and C. K. Ross, Phys. Lett. B **60**, 237 (1976); M. Baldo and L. Ferreira, Phys. Rev. C **59**, 682 (1999).
[69] X. R. Zhou, G. F. Burgio, U. Lombardo, H.-J. Schulze, and W. Zuo, Phys. Rev. C **69**, 018801 (2004).
[70] Z. H. Li, U. Lombardo, H.-J. Schulze, and W. Zuo, Phys. Rev. C **77**, 034316 (2008).
[71] Z. H. Li and H.-J. Schulze, Phys. Rev. C **78**, 028801 (2008).
[72] H. Müther, A. Polls, and R. Machleidt, Phys. Lett. B **445**, 259 (1999).